Morphological changes and riffle-pool dynamics related to flow in a meandering river channel based on a 5-year monitoring period using close-range remote sensing

J. Salmela[1*], E. Kasvi[1], M.T. Vaaja [2], H. Kaartinen[1,3], A. Kukko[2,3], A. Jaakkola[4], P. Alho[1,3]

1. University of Turku, Department of Geography and Geology, FI-200014, Turun yliopisto, Finland, jouni.jsalmela@utu.fi (corresponding author)

2. Aalto University, School of Engineering, Department of Built Environment, P.O. Box 14100, FI-00076 Aalto, Finland

3. Finnish Geospatial Research Institute, Department of Remote Sensing and Photogrammetry, FI-02430, Finland

4. Gaze Inc., USA

Abstract

The maintenance of riffle-pool sequences and morphological changes in the long-term have received little attention in the literature. The aims of this study are to determine morphological changes and riffle-pool maintenance in relation to flow conditions in a meandering river channel over a 5-yr period. Change detection was focused on riffle and pool maintenance in a river reach covering three successive meander bends. Changes in a meandering river channel were studied utilizing detailed digital terrain models and flow data. The results indicated that riffle-pool sequences are maintained by high discharge events and the development of pools and riffles was linked. During high discharges, the riverbed eroded on the concave sides and the inflexion points aggraded, causing riffle–pool sequences, whereas during low discharges, concave sides aggraded and inflexion points eroded, causing pool filling and riffle erosion. While discharge increased, near-bed flow velocities increased faster on the concave sides of the bends than at the inflexion points, becoming higher at a discharge of 8 m^3/s, ~20% of the bankfull discharge. Changes in the three successive meander bends were mainly similar, and the geometry of meandering rivers contributed to the locations of riffles and pools. Pools and riffles were not stable in size and shape, but their longitudinal location remained the same, instead of migrating up and down the channel. Morphological changes occurred in meander bends year-round, but they were non-linear. Annual channel change was not similar from year to year owing to different flow regimes and morphological changes during the previous year. However, seasonal detection revealed similarities between high and low discharge periods between the years. Concave sides of meander bends may act to temporarily store sediment; however, storage is preserved only under the effective hydrological discharge.

Highlights:

- The strongest morphological changes are located on the concave sides of meander bends.

- Riffles and pools are not stable in size and shape, but their longitudinal location remains same.

- Morphological changes are strongly related to discharge and near-bed flow velocity variation.

- Annual morphological change is not linear, owing to different flow regimes and changes during the previous year.

- The riffle–pool sequence is maintained by effective hydrological events, in our study above ~20% of bankfull discharge.

1. Introduction

Meandering riverbeds are characterized by a series of bathymetric highs and lows (i.e., riffles and pools). These riffle-pool sequences (RPS) are typically located in meander bends with pools positioned on the concave side and riffles at inflexion points between two adjacent meander bends (Keller, 1972; Dietrich et al., 1979;). RPSs also occur in straight channels (Leopold and Wolman, 1957) with bed sediment ranging between coarse sand and cobbles (Richards, 1976). The differences in hydrological and bed material conditions over the RPS provide important habitats for aquatic species (Fukushima, 2001; Tonina and Buffington, 2009; Montgomery et al., 2011). Because we lack suitable measurement techniques enabling an adequate spatiotemporal scale, gaps remain in our understanding of the morphological development of pools and riffles over several years. The purpose of our study is to provide new insights into the multi-annual development and maintenance of RPSs in relation to hydraulic conditions using state-of-the-art close-range remote sensing techniques.

Several studies have provided important information about morphological changes in terms of riffle-pool maintenance and sediment-flow interaction. RPS at meander bends are caused by erosion on the concave sides and deposition at downstream inflexion points. The combination of secondary flow structure, skew-induced helical flow and the shifting of the high velocity core (HVC) towards the concave sides of the bends cause erosion rather than sediment deposition at the concave sides (Bathurst et al., 1979; Dietrich and Smith, 1984; Frothingham and Rhoads, 2003; Konsoer et al., 2016a). Sediment transport, from the concave side pools either to inflexion points or to the downstream part of the point bar, has been also attributed to stronger flow velocities and boundary shear stress on the concave side (Keller, 1971; Dietrich et al., 1979; Thompson, 1986) and the decline of flow velocity and stream power at the downstream inflexion point (Bridge and Jarvis, 1976; Pyrce and Ashmore, 2005).

Morphological changes in alluvial rivers can occur either during single floods (Kasvi et al., 2017b) or at low discharges (Riley and Rhoads, 2012). Changes in meander bend morphology may be caused not only by hydrological characteristics, but also changes during the preceding year that influence

subsequent changes (Gautier et al., 2010; Kasvi et al., 2013). However, hydrological events have more influence on morphological changes in meander bend point bars than bend characteristics, such as planform type, radius of curvature and sinuosity (Lotsari et al., 2014).

Several theories on RPS formation and maintenance have been proposed, including various reversal theories (e.g., Andrews, 1979; Carling, 1991; Keller and Florsheim, 1993) and grain size distribution (Hirsch and Abrahams, 1981; Frothingham and Rhoads, 2003). Flow velocity reversal and shear stress reversals have been proposed for riffle-pool maintenance (Keller, 1971; Lisle, 1979). In either mechanism, coarser bed material is concentrated in riffles at high or near bankfull flows owing to stronger flow velocity in pools than riffles. Furthermore, Vetter (2011) stated that RPSs are maintained under the hydraulic conditions of high flows. The RPS maintenance also may be explained by the competence reversal, caused by hydraulic roughness differences between riffles and pools (Carling and Wood, 1994) or transport reversal, the consequence of a different grain size distribution between pools and riffles (De Almeida and Rodríguez, 2011). Transport reversal may occur at considerably smaller discharges than those associated with velocity or shear stress reversal. In addition, Hodge et al. (2013) concluded that pools are more easily eroded than riffles because of looser sediment packing in pools. Their model showed that the threshold shear stress for sediment entrainment is larger in pools and thus velocity reversal is not always necessary for the maintenance of RPS. An alternative hypothesis of riffle-pool maintenance has been provided based on sediment routing (Booker et al., 2001; Milan, 2013). Booker et al. (2001) found that while discharge increases, cross-sectional flow velocity simultaneously increases in pools and decreases on riffles. However, they stated that this flow pattern is too simplistic to explain the maintenance of all riffle-pool sequences and the routing of near-bed velocity away from the deepest parts of pools has implications for sediment transport and the subsequent maintenance of riffle-pool morphology. Milan (2013) proposed that pool maintenance does not require a hydraulic reversal as described in earlier studies, because sediment is predominantly routed onto bars rather than through pools. Wilkinson et al. (2004) proposed a shear stress phase shift theory to explain the maintenance of RPS. The shear stress phase shift allows scour to occur at high flows while deposition occurs at low flows as required for the long-term stability of the morphology. MacWilliams et al. (2006)

stated that the velocity reversal hypothesis does not explain the maintenance of riffle-pool morphology. Instead, pools are maintained by convergent flow at pools caused by the occurrence of an upstream flow constriction. Clifford (1993) argued that RPS are self-maintaining because riffles form an obstacle influencing convergent flows in pools, and thus pool development both up and downstream from the riffle. Also different intensities of turbulence may cause different patterns of sediment entrainment at pools (MacVicar and Roy, 2007; Thompson and Wohl, 2009).

Because of different velocities or shear stresses between riffles and pools, coarser particles settle in riffles and finer particles in pools (Keller, 1971; Hirsch and Abrahams, 1981;). This irregular grain size distribution between riffles and pools also contributes to RPS maintenance because of the low transport capacity in riffles at low flows. Pools may be filled at low flows with fine sediments, but during the next effective discharge sediments will be entrained and the river bed scoured, developing pools at the same locations (Keller, 1971; Andrews, 1979). Buffington et al. (2002) stated that pool scour can be influenced by the volume and calibre of sediment supply. In addition, Vetter (2011) stated that discontinuous sediment supply preserves RPS sequences during low flows.

Thus far, the research of riffle-pool dynamics has mostly focused on gravel bed rivers instead of sand bed rivers, which characterize our study. In addition, most of the studies have focused on the causes of RPS formation and maintenance, instead of long-term behaviour. Although, long-term lateral meander evolution has been studied successfully (e.g., Hooke, 2003) and riffles and pools may be a fundamental prerequisite for meandering (Richards, 1976), the literature lacks studies of the simultaneous exploration of morphological changes and maintenance of RPS along river reaches over several consecutive years. It is not known how morphological changes occur over the years or how the location and volume of pools and riffles change. In addition, it remains unclear whether such changes are similar along a given reach. One of the main reasons for these deficiencies has been the lack of suitable measurement techniques enabling adequate vertical accuracy and precision (Kasvi et al., 2017a). For the most part, previous studies have been carried out with a limited spatiotemporal scale, such as cross-sectional measurements (Schumm, 1963; Ferguson and Ashworth, 1992; Vetter, 2011; Caamaño et al.,

2012), a single transect along a thalweg (Carling and Harriet, 2000), a single meander bend (Riley and Rhoads, 2012; Kasvi et al., 2017b) or a single geomorphic unit (Kasvi et al., 2013) Although, the development of close-range remote sensing techniques has enabled highly detailed riverine surveys (both spatially and temporally) (Alho et al., 2009; Flener et al., 2013; Williams et al., 2014; Kasvi et al., 2015, 2017b), these techniques have not yet been fully utilized in detecting long-term morphological change and RPS maintenance. For example, research with high spatial detail has been limited to the monitoring of a single time period (Williams et al., 2011; Kasvi et al., 2017b) rather than annual and seasonal changes over consecutive years. Both Konsoer et al. (2016b) and Lotsari et al. (2014) studied morphological changes of adjacent meander bends, but their studies did not include the submerged channel morphology that plays an important role in understanding meander bend behaviour. Kasvi et al. (2017b) studied morphological changes of a submerged meander with high spatiotemporal resolution, but only during the rising stage of a flood and at a single meander bend. In addition, Williams et al. (2014) fused mobile terrestrial laser scanning (TLS) and optical bathymetric mapping only to model the topography of a braided river, instead of also analysing morphological changes.

This study aims to determine multi-annual morphological changes and riffle-pool maintenance in relation to flow, which is needed given the dynamic nature of meandering rivers. In addition, our findings contribute the understanding of long-term lateral meander evolution. We seek answers to the following research questions:

1. How do meander bends, riffles and pools behave under different flow conditions?
2. How do morphological changes coincide among consecutive meander bends and years?

Detailed measurements of morphological changes and flow stages over five consecutive years are provided for a ~1.3 km river reach covering three meander bends. To accomplish the analyses, we compared flow regime, including discharge variation and near-bed flow velocities, and morphological changes in three meander bends. As far as the authors know, this is the first study to examine channel changes and riffle-pool maintenance over several consecutive years along a meandering river reach in such high spatial detail.

2. Study area

The study was performed in the subarctic meandering Pulmankijoki River, located in northern Finland (Fig. 1). The river consists of mobile sandy bed sediment (D_{50} = 0.2 – 3 mm; Kasvi, 2015) deposited during the retreat of the continental ice (Mansikkaniemi and Mäki, 1990). The river is characterized by riffles, pools and bars. Discharge typically varies between 2 m³/s and 10 m³/s during open-water periods, but discharge may exceed 70 m³/s during the snowmelt period in spring. The bankfull discharge is 41 m³/s (Kasvi et al., 2013). Under ice cover, the discharge remains below 1 m³/s (Lotsari et al., 2017). The length of the studied reach is approximately 1.3 km with a gradient of 0.0003, and it consists of three meander bends and one straight reach. The drainage area is about 480 km² and consists mainly of moors and peatbogs, typical for high altitudes. There is no human presence in the drainage basin. The latest recorded meander cut-off along the Pulmankijoki River occurred in 1980 (Mansikkaniemi and Mäki, 1990). The river flows into Lake Pulmankijärvi, approximately 1.5 km downstream from the study reach. Because the study site is only 1.5 km upstream of Lake Pulmankijärvi, the backwater effect during spring floods may decrease flow velocities and stream power at meander bends as Kasvi et al. (2017b) have described. The study reach's homogenous, non-vegetated river bottom and clear, shallow water offer an ideal environment for close-range remote sensing applications.
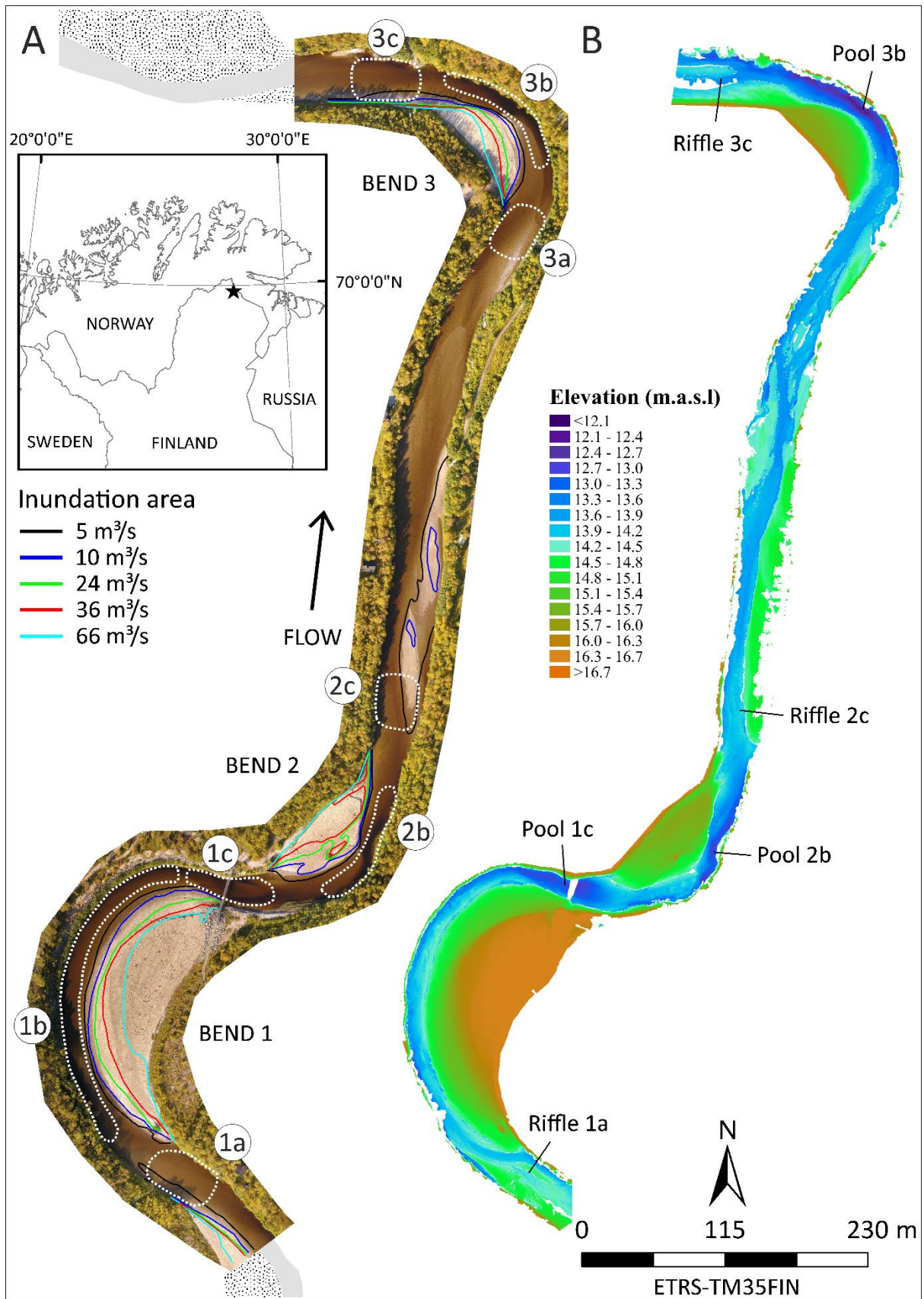
Figure 1. The study reach (A) and location of pools and riffles in the beginning of the study (B). (A) The study reach covers 1.3 km of the Pulmankijoki River, including three meander bends (1 – 3) and a

straight reach. The study reach is mainly in its natural form except at bend 1, which has artificial bank protection on the outer bank and a suspension bridge located at the meander exit. Inundation areas during various discharges (5 – 66 m³/s) have been visualized at each bar. The background is a UAV image from autumn 2017, when discharge was approximately 8 m³/s. Areas where near-bed flow velocities were averaged for analysis are marked with a dashed white line (1a – 3c). 1a = bend 1 entrance, 1b = bend 1 concave side, 1c = bend 1 exit, 2b = bend 2 concave side, 2c = bend 2 exit, 3a = bend 3 entrance, 3b = bend 3 concave side and 3c = bend 3 exit. (B) Pools and riffles marked on the Digital Terrain Model (DTM) of autumn 2013.

Each meander bend has different characteristics (Table 1). Bend 1 is a simple asymmetric bend with artificial bank protection to stabilize the channel. Bank protection consist of approximately 0.1 – 0.5 m-diameter piled stones. A suspension bridge is also located at the bend 1 exit. Bend 3 is preceded by a long (400 m), relatively straight reach, whereas the other bends are preceded by meander bends (Fig. 1).

Table 1. Characteristics of examined meander bends. The locations of the bends are marked in Fig 1.

	Bend 1	Bend 2	Bend 3
Sinunosity	1.6	1.2	1.4
Radius of curvature at the apex	120 m	47 m	110 m
Width (low flow)	22 m	15 m	19 m
Width (bankful)	100 m	65 m	60 m
Planform type	Simple asymmetric	Simple symmetric	Simple symmetric

3. Data collection and processing

Our interest is in aggradation and erosion rates in terms of riffle-pool behaviour and their relation to variation of discharge. Thus, we combine close-range remote sensing techniques, including the use of mobile laser scanning (MLS), unmanned aerial vehicle (UAV) photogrammetry and an acoustic Doppler current profiler (ADCP) to evaluate whether erosion or deposition occurs. Our seven seamless high-resolution (six 0.2 m and one 1.0 m) DTMs for 2013 – 2017 provide change detection for four annual, two open-water (summer) and two ice-covered (winter) periods, as well as one whole-study period.

3.1. Flow characteristics

3.1.1. Hydrographs

Hydrographs for each unfrozen period between 2013 and 2017 were calculated based on the relationship between the discharge measurements and water level. Water level fluctuation was monitored using four water pressure sensors (Solinst Levelogger Gold, Model 3001; accuracy 0.05% [Solinst]) along the study reach from mid-May until mid-September each year. Data were recorded in 15-min intervals. Sensors were installed at the beginning of each spring campaign and collected at the end of each autumn campaign. To compensate for air pressure, one air pressure sensor (Solinst Barologger) was installed at the study site. In addition, during both the spring and autumn field campaigns, the water level was measured next to each sensor using a real-time kinematic global navigation satellite system (RTK-GNSS; Trimble R8 or R10; accuracy vertical: 0.05 m, horizontal 0.03 m) at different flow stages. RTK-GNSS measurements were used to determine water elevation above sea level and monitor the potential vertical movement of the sensors on the river bottom. Discharge measurements were conducted next to water pressure sensors using ADCP (see details in Section 3.1.2) in the upstream and downstream parts of the study reach during spring (flood) and autumn (low stage) field campaigns. Discharge measurements and water levels were cross plotted to create a regression curve and formula for each hydrograph individually.

3.1.2. Near-bed flow velocities

Flow measurements were conducted during each field campaign in spring and autumn, 14 times during the five-year study period (spring 2013 – autumn 2017). Measurements were conducted during a variety of discharges. We used several platforms for our ADCP sensors (Sontek M9 and S5) based on the flow conditions during the five-year study period. The ADCP sensor was mounted either on remote-controlled mini boat (see a more detailed description in Kasvi et al., 2017) or kayak during low flows and on a hydroboard attached with a pole to a motorboat bow during high flows (Fig. 2). On each platform, the ADCP sensor was mounted in front of the boat to avoid any disturbances to the flow field caused by the hull. The ADCP sensor was moved in a zig-zag cross-sectional pattern in the upstream direction and, in the end, parallel to the flow to cover plausible blank areas (see e.g., Flener et al., 2015). The measurement frequency was 1 Hz, and the number of samples collected during each measurement campaign was related to inundation area and the density of the zig-zag style cross-sectional pattern.
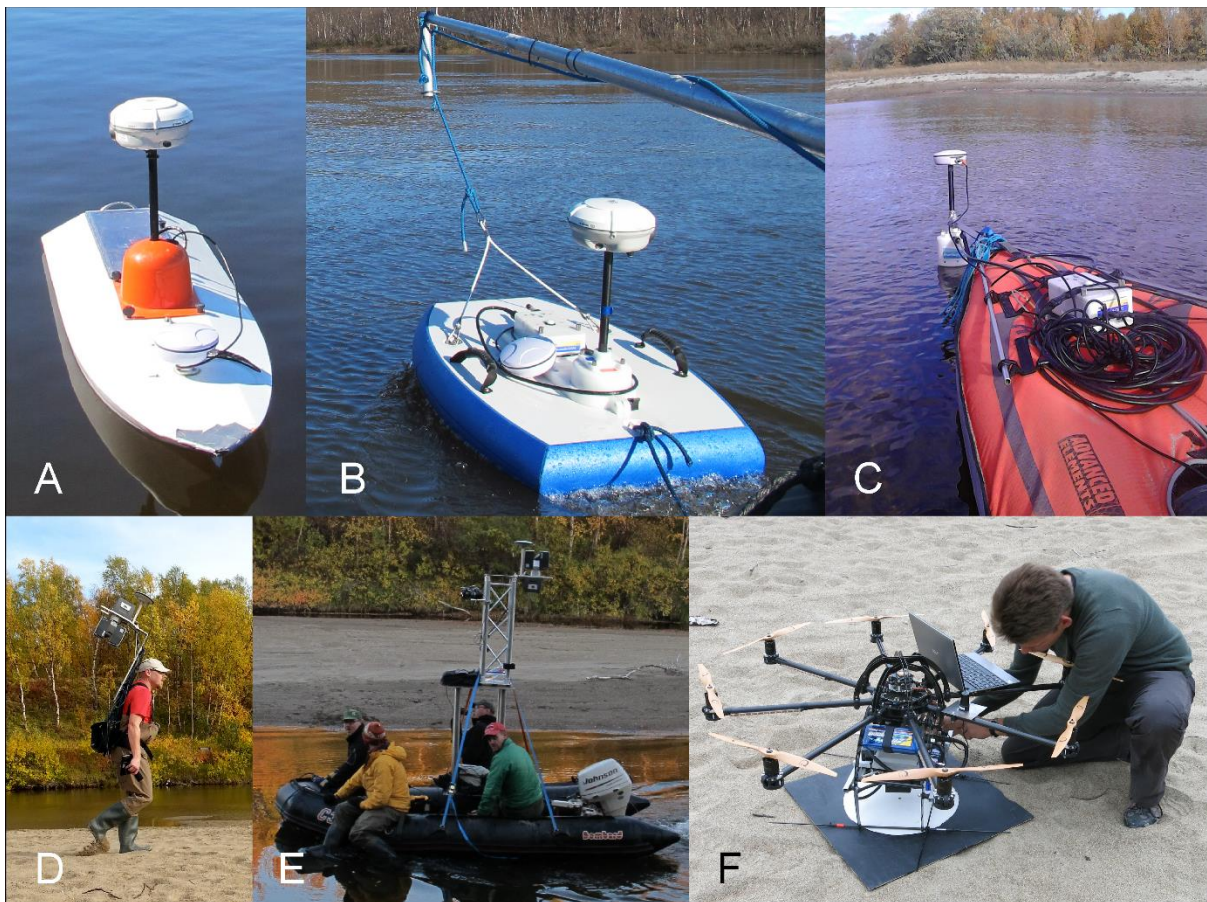
Figure 2. Field measurements setups. Flow measurements were conducted using three platforms: (A) remote-controlled mini-boat, (B) hydroboard and (C) kayak. For MLS measurements, either (D) a backpack, (E) boat or (F) UAV was used. Laser scanner sensors were located approximately 2 m above the ground or water level in the backpack and boat set-ups, whereas UAV set-up sensors were located beneath the UAV.

Positioning of the ADCP sensor was based on the differential GPS (dGPS; Hemisphere A10) provided by the manufacturer. Typical horizontal accuracy for the dGPS is less than 1 m (SonTek, 2010). Each dataset collected contained samples with lower GPS accuracy, which were removed during data processing. In very shallow waters (<0.2 m) (e.g., near shorelines), data was not collected because of the sensor's inability to measure shallow water. Flow velocities were extracted from the dataset using the boundaries of predefined areas 1a – 3c (Fig. 1) next to each bend. The deepest measured cell of each flow velocity sample was selected to represent the near-bed flow velocity. Finally, average near-bed flow velocity for each area and for the entire study reach was calculated (Fig. 3). In addition, flow samples from spring 2017 at 10 m³/s discharge were interpolated into a 1 m resolution surface model and nine cross sections were extracted from the zig-zag style pattern to visualize the spatial variation of near-bed flow velocities and compare near-bed and depth-averaged flow velocities along the meander bends.

3.2. Measuring and modelling the river channel geometry

3.2.1. Data acquisition and riverine DTMs

To create DTMs, we measured the elevation of inundated and non-inundated channels using MLS, UAV photogrammetry or echo sounding (Fig. 3). MLS and UAV photogrammetry-based structure-from-motion (SfM) measurements were used to create DTMs for non-inundated areas, whereas UAV images and echo sounding were used for the inundated areas. MLS was used between 2013 and 2016, but it was replaced by SfM in 2017 (Table 2). UAV images were used for optical bathymetric modelling between 2013 and 2015 but were replaced by echo sounding from 2016 onwards. The techniques were selected based on water level and turbidity, as well as the techniques available during each field

campaign. Bankfull discharge and, thus, point bar inundation occurred mainly during the spring floods. Outside the spring floods, water level remained relatively low, inundating only the main channel.

To combine non-inundated DTMs and bathymetric models, water levels were measured using RTK-GNSS next to water pressure sensors along the study reach simultaneously with the acquisition of bathymetric data. Based on the water level measurements, the water surface was interpolated for the entire study reach. Bathymetric values were extracted from the interpolated water surface to calculate the elevation of the riverbed. Water level remained stable (vertical change less than $\pm$ 0.02 m) during the acquisition of bathymetric data .
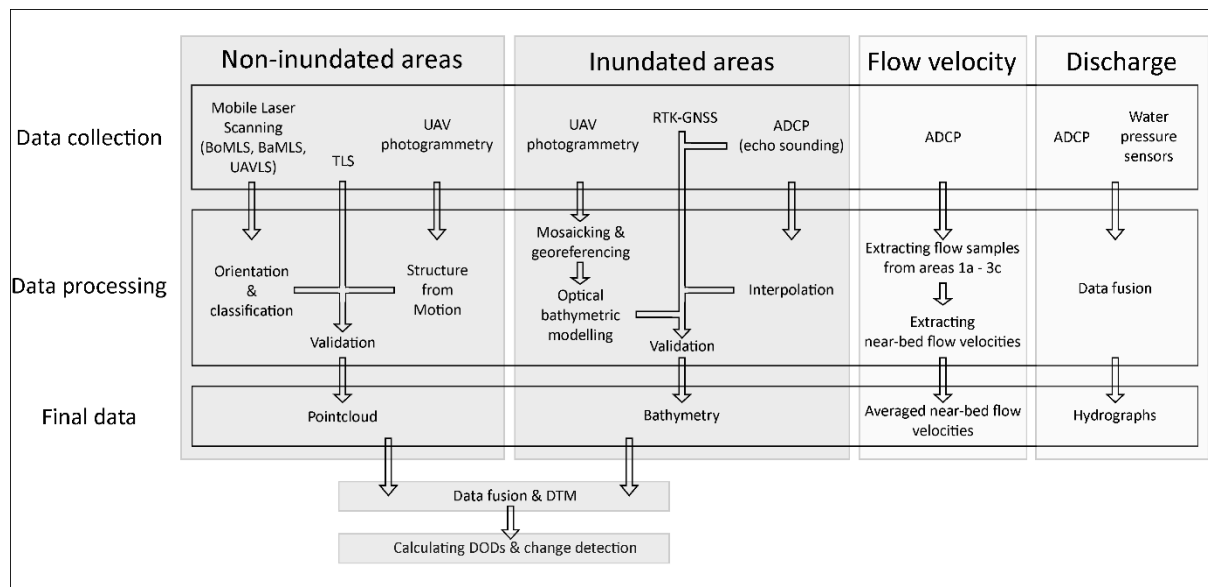
Figure 3. The process of DTM creation and flow and discharge measurements during the 5-yr study period. Topography measurements for non-inundated areas were based on either MLS or UAV photogrammetry. Topography of inundation areas was modelled based on either UAV photogrammetry or interpolation of echo-sounding measurements.

		2013 autumn		2014 autumn		2015 autumn		2016 spring		2016 autumn		2017 spring		2017 autumn	
		Non-inundated	Inundated	Non-inundated	Inundated	Non-inundated	Inundated	Non-inundated	Inundated	Non-inundated	Inundated	Non-inundated	Inundated	Non-inundated	Inundated
Resolution		BaMLS 20 000 pts/m²	UAV image 0.05 m	BoMLS 700 pts/m²	UAV image 0.05 m	UAVLS 700 pts/m²	UAV image 0.05 m	-	ADCP 3.7 pts/m²	BaMLS 35 000 pts/m²	ADCP 3.66 pts/m²	SfM 0.03 m	ADCP 0.64 pts/m²	SfM 0.03 m	ADCP 0.59 pts/m²
Date		11/12.9	12.9	19.9	19.9	16.9	15.9	11	20.5	9.9	8.9	3.6	30 - 31.5	7.9	7.9
Discharge m³/s		2	2	2	2	2	2	11	11	8	8	11	10	4	4

Table 2. Details of data collection methods, original ground resolution and point density for each field campaign. Higher ADCP point density measurements in 2016 were achieved owing to the use of different measurement technique. In 2016, we used HydroSurveyor software, which enables the ADCP to measure water depth simultaneously with five beams instead of one. In 2017, RiverSurveyor Live software was used, which employs only one beam for depth measurements.

3.2.2. Non-inundated areas

MLS surveys were conducted during the low-flow stage in the autumn field campaigns between 2013 and 2016. Three MLS configurations were used: backpack (BaMLS, 2013 and 2016), boat (BoMLS, 2014) and UAV (UAVLS) (2015). For a more detailed description of these MLS configurations, see Jaakkola et al. (2017), Lotsari et al. (2015) and Nylén et al. (in press). MLS data was collected either by walking (backpack) along the study reach or floating (boat) downstream in the river (Fig. 2). For UAVLS, two flight lines (i.e., back and forth) were flown at an altitude of 90 m. During the MLS surveys, spherical reference targets (SRTs) were placed around the study reach to evaluate system calibration accuracy. SRT location was measured using RTK-GNSS. Point clouds were georeferenced with GNSS-IMU sensors mounted on MLS systems and vegetation was removed to determine the ground surface using the method developed by Axelsson (2000) (Fig. 3). Point clouds were resampled into 0.2-m point densities based on the average height value of the nearest points and converted into 0.2-m raster grids.

MLS was replaced by SfM in 2017. Data for SfM (UAV images) was collected by flying at altitudes of 90 m (nadir), 70 m (nadir) and 50 m (off-nadir, 30° off vertical) above the ground during the spring and autumn 2017 field campaigns. Two flight lines, the first along the right bank and the second along the left bank, were used at each altitude. Time-lapse interval was two seconds. Ground control points (GCPs)

were placed on the right and left banks, and their locations were measured using RTK-GNSS. Image mosaicking and georeferencing were performed to create point clouds and DTMs. Original ground resolution for both DTMs was 0.03 m (Table 3), but this was resampled into a 0.2-m raster grid. For a more detailed description of SfM data acquisition and processing, see Kasvi et al. (2019).

3.2.3. Inundated channel section

UAV images were collected during the autumn 2013 – 2015 field campaigns. Each year, image acquisition was undertaken at a flying altitude of 90 m. GCPs were placed on both sides of the river along the reach, and their locations were measured using RTK-GNSS. UAV images were mosaicked and georeferenced based on GCPs (Fig. 3). The final horizontal ground resolution for each orthomosaic was 0.05 m and the resolution was later resampled at 0.2 m for optical bathymetric modelling. The water surface, excluding shadow areas, was extracted visually from the orthophotos. For a more detailed description of the UAV image processing procedure, see Flener et al. (2013).

Our optical bathymetric modelling was based on a method originally developed by Lyzenga (1981) and later successfully modified by (Flener, 2013). Flener (2013) stated that deep water reflectance can be neglected in clear, shallow rivers without any effect on the modelling results. Optical bathymetries were modelled based on the pixel brightness value of the red band only instead of the band ratio. Reference and validation depths were measured simultaneously with flow measurements using ADCP (Fig. 3). Depth measurements were selected at various locations along the study reach to minimize disturbances on UAV images, such as those caused by sunlight. Reference depths and pixel value (red band) were cross plotted and a linear transform was used to model depths for each pixel. In 2013, 2014 and 2015, the total number of reference points was 2818, 3041 and 580, respectively. For a more detailed description of the optical bathymetric modelling procedure, see Kasvi et al. (2019).

From the spring of 2016 onwards, bathymetric models were calculated based on ADCP measurements only. Two different platforms, a remote-controlled mini boat (2016) and a kayak (2017), were used for

ADCP (Fig. 2). An ADCP M9 sensor was used in 2016, and an S5 sensor was used in 2017. Depth measurements were collected simultaneously with flow data (see Section 3.1.2).

In 2016, depth was measured using Hydrosurveyor software, which enables water depth measurements using five sensor beams (including one vertical and four tilted beams). RiverSurveyor Live software, which employs only one beam for depth measurement, was used in 2017. Depth measurement density for each campaign is listed in Table 2.

Because of the lack of ADCP sensors to measure shallow water (<0.2 m), shoreline points at each point bar were extracted from MLS or SfM point clouds and added to depth sample datasets before bathymetric interpolation. This allowed us to model shallow areas near point bar margins instead of leaving them blank. For example, the horizontal distance between the shoreline points and depth samples was approximately 2.5 – 3.5 m in the spring of 2017. Depth samples were interpolated with a triangulated irregular network (TIN), and the TIN model was later rasterized to create a bathymetric model. The TIN method was found to be the most suitable compared to other interpolation methods, such as kriging and inverse distance weighting (IDW) and gave us the best results when bathymetric models were validated. Validation data were measured using either ADCP or RTK-GNSS (Table 3). The resolution of the final bathymetric models was 0.2 m, except in the spring of 2016 (1.0 m) when the topographic data of non-inundated areas was not collected and the bathymetric data was not needed to rasterize into same 0.2 m resolution as non-inundated areas.

3.2.4. Accuracy assessment

Instead of seamless DTMs, accuracy assessments were performed separately for each model owing to differences in the measuring techniques and accuracies (Table 3). The accuracy assessment for boat- and backpack-based MLS techniques is based on the previous work of Flener et al. (2013) at the same study area, which was found suitable for our purposes and therefore not re-assessed in this study. Validation of SfM (autumn 2017) and UAVLS (autumn 2015) models was based on TLS measurements located 1 km upstream from the study reach. TLS data were collected at the same time during field

campaigns. MLS and SfM measurements covered the larger extent of the Pulmankijoki River, but those areas were excluded from this study area. Validation data were not available for SfM in spring 2017, but we expect the accuracy to be same as autumn 2017 because we used the same measurement technique (see Kasvi et al., 2019). TLS data were selected for validation because it represents land surface at the highest available quality (Schürch et al., 2011) and provides large spatial coverage and resolution.

Optical bathymetric models were validated against ADCP-based depth measurements along the study reach. A total of 1770, 120 and 491 validation depths were completed in 2013, 2014 and 2015, respectively (Table 3). Whereas optical bathymetries were validated against depth measurements, ADCP-based bathymetric models were validated against elevation values above sea level. Validation data for ADCP-based models were collected using ADCP or RTK-GNSS at various locations along the study reach. ADCP depth values were converted into elevation values based on RTK-GNSS water level measurements along the study reach. The total number of validation points for ADCP-based bathymetry was 288 (spring 2016), 64 (autumn 2016), 351 (spring 2017) and 129 (autumn 2017) (Table 3).

For each model, correlation coefficient (R), R^2 value, mean error (ME) and standard deviation of error (SDE) were calculated (Table 3).

Table 3. Accuracy assessment of each model. Models were validated using ADCP, RTK-GNSS or TLS measurements. Optical bathymetries were validated using depth (d) values, and ADCP-based bathymetries were validated using elevation (e) values. MLS and SfM data were validated using TLS measurements. BaMLS = Backpack Mobile Laser Scanning, BoMLS = Boat Mobile Laser Scanning, UAVLS = Unmanned Aerial Vehicle Laser Scanning, BM = bathymetric model, ADCP_CS = ADCP cross-sections, ME = mean error and SDE = standard deviation of error.

	2013		2014		2015		2016			2017			
	autumn		autumn		autumn		spring	autumn		spring		autumn	
	BaMLS*	BM (optical)	BoMLS	BM (optical)	UAVLS	BM (optical)	BM (ADCP)	BaMLS*	BM (ADCP)	SfM	BM (ADCP)	SfM	BM (ADCP)
R		0.86		0.92	1.00	0.85	1.00		0.98	**	0.99	0.99	0.94
R2		0.74		0.85	1.00	0.72	0.99		0.95	**	0.98	0.98	0.89
ME (m)		-0.04		0.11	0.03	-0.02	-0.05		0.04		0.05		-0.03
SDE (m)		0.21		0.18	0.05	0.15	0.06		0.06		0.06		0.13
n		1770		120	196 955	491	288		64		351		129
Validation data	TLS	ADCP (d)	TLS	ADCP_CS (d)	TLS	ADCP (d)	ADCP_CS (e)	TLS	RTK-GNSS		ADCP_CS (e)	TLS	ADCP (e)/RTK-GNSS

* Validation data was not collected in this study but for MLS accuracy analysis see Flener et al. 2013

** Validation data was not collected

For change detection purposes, the level of significant change detection (LoD) was calculated according to Lotsari et al. (2014):

$$\sigma_c = t(\sigma_1^2 + \sigma_2^2)^{1/2} \tag{1}$$

where σ_1 is the standard deviation between the validation and model points of the first dataset, and σ_2 is the standard deviation between the validation and model points of the second dataset. A t-value of 1.96 ($2\,\sigma$) was selected, which means that the confidence limit is 95%. Owing to the lowest model accuracies of the bathymetric models (Table 3), LoDs were calculated based on the validation data at inundated areas (Table 4). However, the LoD value does not represent the accuracy of non-inundated areas because of the different measurement techniques and accuracies.

Table 4. Quality of DTMs and change analysis. A = autumn and S = spring.

DoD	σ^2_1	σ^2_2	LoD (95% confidence limit (m))
A13 - A14	0.04	0.03	0.54
A14 - A15	0.03	0.02	0.46
A15 - S16	0.02	0.00	0.32
S16 - A16	0.00	0.00	0.16
A15 - A16	0.02	0.00	0.33
A16 - S17	0.00	0.00	0.17
S17 - A17	0.00	0.00	0.29
A16 - A17	0.00	0.00	0.29
TOTAL	0.04	0.01	0.49

3.3. Building seamless riverine DTMs and calculating DoDs

Seamless DTMs for each field campaign were created by combining bathymetric models and dry-bed terrain models for each period except spring 2016, when the topography of non-inundated areas was not measured. Some blank areas exist in the seamless DTMs owing to disturbing shadows in the bathymetric models caused by canopies or steep river banks. In addition, some parts of the ADCP-based bathymetries were not covered with a desired spatial density because of poor GNSS signals next to the steep river banks. Those depth samples were deleted from the datasets before the further processing. Blank areas, especially near concave sides, were not interpolated because of possible distortion caused by the interpolation method. For example, concave sides may have become more shallow than they appeared.

After riverine DTMs were created, we calculated annual and seasonal DoDs. In total, nine DoDs were calculated: four annual, two winter and two summer DoDs, as well as one for the entire study period.

5. Results and discussion

5.1. Discharge regime and near-bed flow velocities

A spring flood between May and June and a lower discharge period during the summer characterized each open-water period (Fig. 4). Snow melt between May and June caused the highest discharges during each open-water period, whereas rainfall associated discharge peaks were recorded during the summers. Unfortunately, the spring flood was not recorded in 2015 and 2016 and thus highest discharges peaks were not available. In 2013, discharge remained above bankfull discharge (41 m³/s) for 11 days with the peak discharge around 58 m³/s. In 2014, discharge exceeded the bankfull discharge twice during the spring flood, on 22 May (43 m³/s) and 1 June (43 m³/s). During the 2017 spring flood, discharge remained above the bankfull discharge for 18 days with the peak discharge around 80 m³/s.
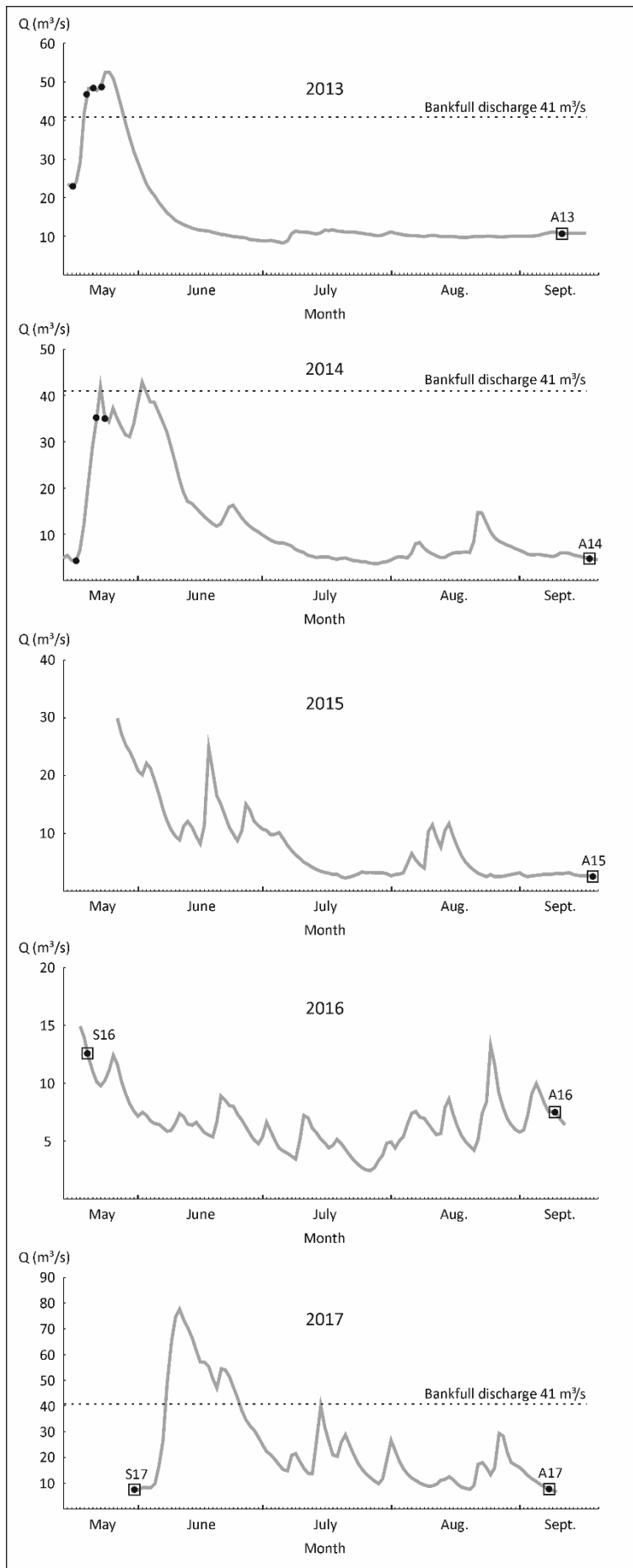
Figure 4. Hydrographs for open water periods during the study period. Near-bed flow measurements and DTM data collection marked with dots and squares respectively. A= autumn and S = spring.

According to our data, near-bed flow velocities increased with discharge at each part of the meander bends (1a – 3c) along the study reach (Table 5). The strongest near-bed flow velocities appear on the concave sides of bends, which is consistent with earlier studies (Leopold and Wolman, 1960; Bridge and Jarvis, 1976; Bathurst et al., 1979; Dietrich et al., 1979; Dietrich and Smith, 1984; Frothingham and Rhoads, 2003; Blanckaert, 2010;). In addition, the strongest flow velocities were located at the bend 1 exit. The near-bed flow velocities were, at their highest, >1.0 m/s when flow was close to the bankfull discharge, either at 35 m³/s (2014) or 58 m³/s (2013). The lowest near-bed flow velocities (0.21 – 0.33 m/s)

were also located on the concave sides of each bend and at the bend 1 exit during low discharge. Near-bed flow velocities increased faster on the concave sides than at the exits and entrances to bends, except near the bend 1 exit, indicating the occurrence of near-bed reversal between concave sides and exits and entrances. For example, between discharges of 2 and 58 m³/s, near-bed flow velocities increased 0.92 m/s at the concave side of bend 3 and 0.49 m/s at the bend 3 exit (Table 5). Occurrence of near-bed reversal in meander bends is most likely related to secondary flow structure and shifting of HVC towards concave side of the bend (Dietrich et al., 1979; Thompson, 1986; Caamaño et al., 2012). In addition, our data show that there is variation in near-bed flow velocities at the same discharges (Table 5). This variation may be explained by the differences in bed elevation between the data acquisition periods. Occasional flow pulses and water turbulence may also explain the variation.

Table 5. Average near-bed flow velocities and depths along the study reach. Bold values indicate situations in which the average near-bed flow velocity was higher at entrances and exits than on the adjacent concave sides of the bends. The highest and second highest near-bed flow velocities at each location are highlighted in dark grey. The number (1a – 3c) in the column name refers to the location in Fig. 1. N = number of samples.

Date	Q (m³/s)	Related to flood	1a) Bend 1 entrance			1b) Bend 1 concave side			1c) Bend 1 exit			2b) Bend 2 concave side			2c) Bend 2 exit			3a) Bend 3 entrance			3b) Bend 3 concave side			3c) Bend 3 exit		
			N-b flow velocity (m/s)	Depth (m)	n	N-b flow velocity (m/s)	Depth (m)	n	N-b flow velocity (m/s)	Depth (m)	n	N-b flow velocity (m/s)	Depth (m)	n	N-b flow velocity (m/s)	Depth (m)	n	N-b flow velocity (m/s)	Depth (m)	n	N-b flow velocity (m/s)	Depth (m)	n	N-b flow velocity (m/s)	Depth (m)	n
3.3.2014	0.63*	-																0.04*			0.15*					
4.2.2015	0.67*	-																0.15*			0.42*					
10.9.2013	2	-	**0.52**	0.38	107	0.33	0.60	1 085	0.21	1.32	557	0.30	0.85	504	**0.49**	0.38	20	**0.40**	0.34	77	0.24	1.15	871	**0.52**	0.45	62
18.9.2014	2	-	**0.54**	0.38	114	0.36	0.48	894	0.17	1.11	516	0.35	0.79	98	**0.44**	0.38	7	**0.44**	0.38	54	0.40	0.71	375	0.37	0.44	175
17.9.2015	2	-	**0.58**	0.35	94	0.40	0.46	621	0.31	0.54	269	0.30	0.90	353	**0.39**	0.33	83	**0.50**	0.53	51	0.45	0.49	235	0.30	0.47	251
7.9.2017	4	-	0.43	0.39	205	0.52	0.65	2 215	0.35	0.94	900	0.36	0.98	1 348	**0.53**	0.43	376	0.42	0.51	385	0.45	1.01	1 658	0.31	0.70	794
17.5.2014	8	Before spring flood	0.62	0.53	158	0.64	0.88	523	0.36	1.59	159	0.50	1.21	257	**0.67**	0.60	140	**0.62**	0.52	108	0.50	1.27	167	**0.60**	0.57	407
8.9.2016	8	-	.	.		0.51	0.84	1 880	0.51	0.89	484	0.53	0.95	709	0.51	0.63	362	0.48	0.64	416	0.56	1.05	882	0.49	0.68	62
30.5.2017	10	Before spring flood	0.48	0.57	954	0.57	0.97	2 684	**0.59**	0.98	892	0.65	1.05	1 110	0.60	0.61	537	0.51	0.66	829	0.55	1.19	1 642	0.48	0.77	955
20.5.2016	10	Falling limb	0.49	0.67	188	0.53	1.22	2 920	0.42	1.69	979	-	-	-	-	-	-	0.35	0.93	1 104	0.44	1.80	1 408	0.42	0.89	244
15.5.2013	21	Before spring flood	0.61	0.81	204	0.68	1.37	415	**0.78**	1.46	246	0.77	1.50	178	0.61	0.72	103	0.58	0.99	137	0.68	1.73	243	0.54	1.03	360
22.5.2013	34	Rising limb of 2nd peak	0.85	1.64	92	0.91	2.33	229	0.88	2.36	98	0.86	2.78	113	**0.90**	1.56	64	0.73	2.00	124	0.74	2.94	196	**0.78**	1.89	120
21.5.2014	35	Rising limb	0.83	1.22	295	**1.00**	1.86	234	0.95	2.23	118	**1.07**	2.08	148	0.93	1.21	84	**0.94**	1.36	115	1.12	2.20	194	**0.93**	1.29	135
23.5.2014	35	Between two peaks	0.85	1.21	131	0.93	1.77	259	0.87	2.31	103	1.02	2.14	162	0.83	1.24	97	0.85	1.45	95	1.05	2.21	158	0.93	1.33	116
20.5.2013	46	Falling limb of 1st peak	**0.91**	1.75	102	0.92	2.38	315	**1.08**	2.64	106	0.99	2.58	150	0.87	1.54	103	0.78	1.96	126	0.89	2.84	301	0.78	1.81	129
18.5.2013	58	Rising limb of 1st peak	**0.95**	1.82	96	0.99	2.32	167	**1.14**	2.63	93	0.96	2.40	92	0.96	1.49	94	0.91	1.81	175	1.16	2.53	322	1.01	1.67	126

*Lotsari et al. 2017

Our data show that the near-bed flow velocity becomes higher at concave sides than at bend exits and entrances, where pools and riffles were located, respectively, at approximately 20% of bankfull (~8 m³/s). Near-bed flow velocity remains lower at concave sides only during small discharges (<8 m³/s). This might be caused by weak secondary flow on concave sides during low discharge or the narrowing of wet channel width at inflexion points. For example, strong riffle or side bar development at inflexion points increases the bed elevation, and thus the inflexion point may be only partly inundated at low discharges. Flow becomes routed along one side of the channel. This convergent flow pattern at low flows increases near-bed flow velocities owing to narrowing of the wet channel width. In addition, at moderate and high discharges, water flow diverges along the entire active channel at inflexion points, decreasing the near-bed flow velocities.

The HVC of near-bed flow was located next to the concave bank at each bend during moderate flows (10 m³/s) (Fig. 5), when the near-bed flow velocity exceeds 0.8 m/s at each bend. A total of nine cross-sectional measurements (extracted from the zig-zag style measurement pattern) show that the near-bed flow velocity was higher than the depth-averaged flow velocity, especially at cross sections 2, 5 and 8, located at bend apex's, next to concave sides (Figs. 5 and 6). In addition, the occurrence of

secondary flow can be seen in cross sections 3, 5 and 8, where both near-bed and depth-averaged flows are not parallel to primary flow (dashed squares in Fig. 5). The near-bed velocity is higher than the depth-averaged flow velocity near the concave sides of the bends, indicating the secondary flow pattern (Fig. 6). These results pertaining to HVC location and secondary flow are consistent with previous studies at the same reach (Kasvi et al., 2013; Lotsari et al., 2014).
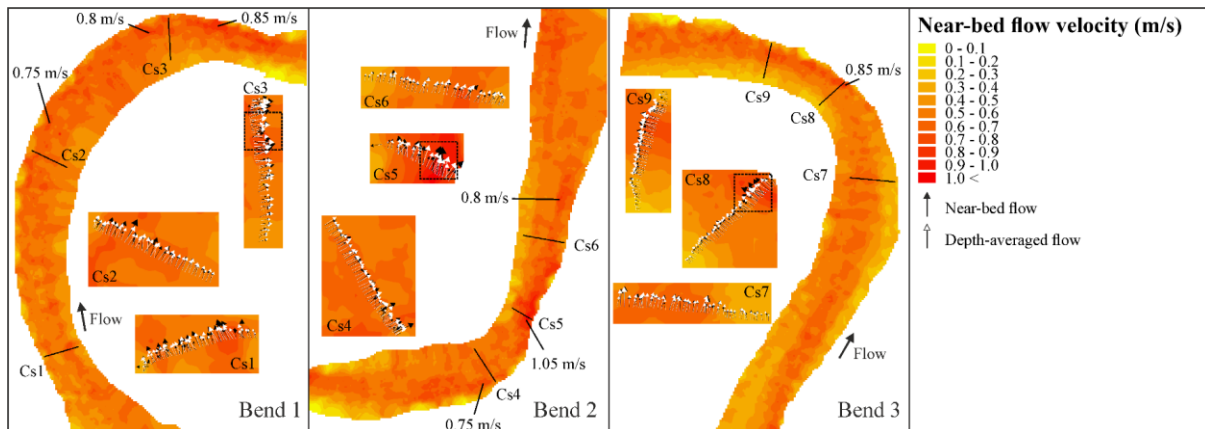

Figure 5. Near-bed and depth-averaged flows at each bend. Near-bed flow velocity is visualized in the background and both near-bed and depth-averaged flows are marked in cross sections (Cs) 1-9. Dashed squares at cross sections highlight the secondary flow.
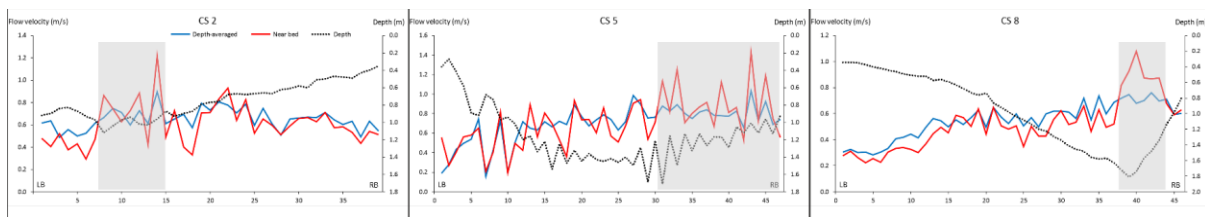
Figure 6. Comparison of near-bed and depth-averaged flow velocities at cross sections 2, 5 and 8 located at the apex of the bends. Grey areas highlight the situation where near-bed flow velocity is higher than depth-averaged. LB = left bank and RB = right bank.

5.2. Morphological changes over different discharge and flow conditions

Morphological changes are strongly related to discharge and near-bed flow variations between concave sides and inflexion points. Periods of high and low discharge have opposite effects on channel change.

Our finding is consistent with the results of Andrews (1979) who stated that sections that scour and fill at high flows tend to fill and scour at low flows, respectively. Erosion was strongest on the concave sides of the bends during high discharges, and deposition was strongest at the same locations during low discharges. For example, during the winter of 2016 (including the spring flood), erosion was strongest on the concave sides of the bends (bend 1 = -0.8 m, bend 2 = -1.0 m and bend 3 = -1.2 m; these values indicate the strongest vertical change at each area measured) and also at the bend 1 exit (-1.6 m) (Table 6 and Fig. 7), causing pools to develop at each location (see the appendix). Simultaneously, the entrances of bends 1 (0.4 m) and 3 (0.3 m) and the exits of bends 2 (0.5 m) and 3 (0.5 m) experienced deposition. These changes were most likely caused by near-bed flow velocity reversal during the spring flood. Discharges and near-bed flow velocities probably remained small (see Lotsari et al.`s (2017) study of the same reach) during the winter before the spring flood, while the river was covered by ice, causing only minor changes in bed elevation (see A16 – S17 in Fig. 7). This assumption is supported by the study of Kasvi et al. (2017) at the same river reach. They found that erosion was strongest on the concave side of a meander bend during the beginning of a flood's rising stage when the point bar was not yet inundated. In addition, the occurrence of the strongest bed shear stresses, maximum velocity core and bank erosion in bends have been found along the outer bank immediately downstream of the bend apex (Leopold et al., 1964: 299 - 301; Bathurst et al., 1979; Dietrich and Smith, 1984; Knighton, 1998: 219; Konsoer et al., 2016a).
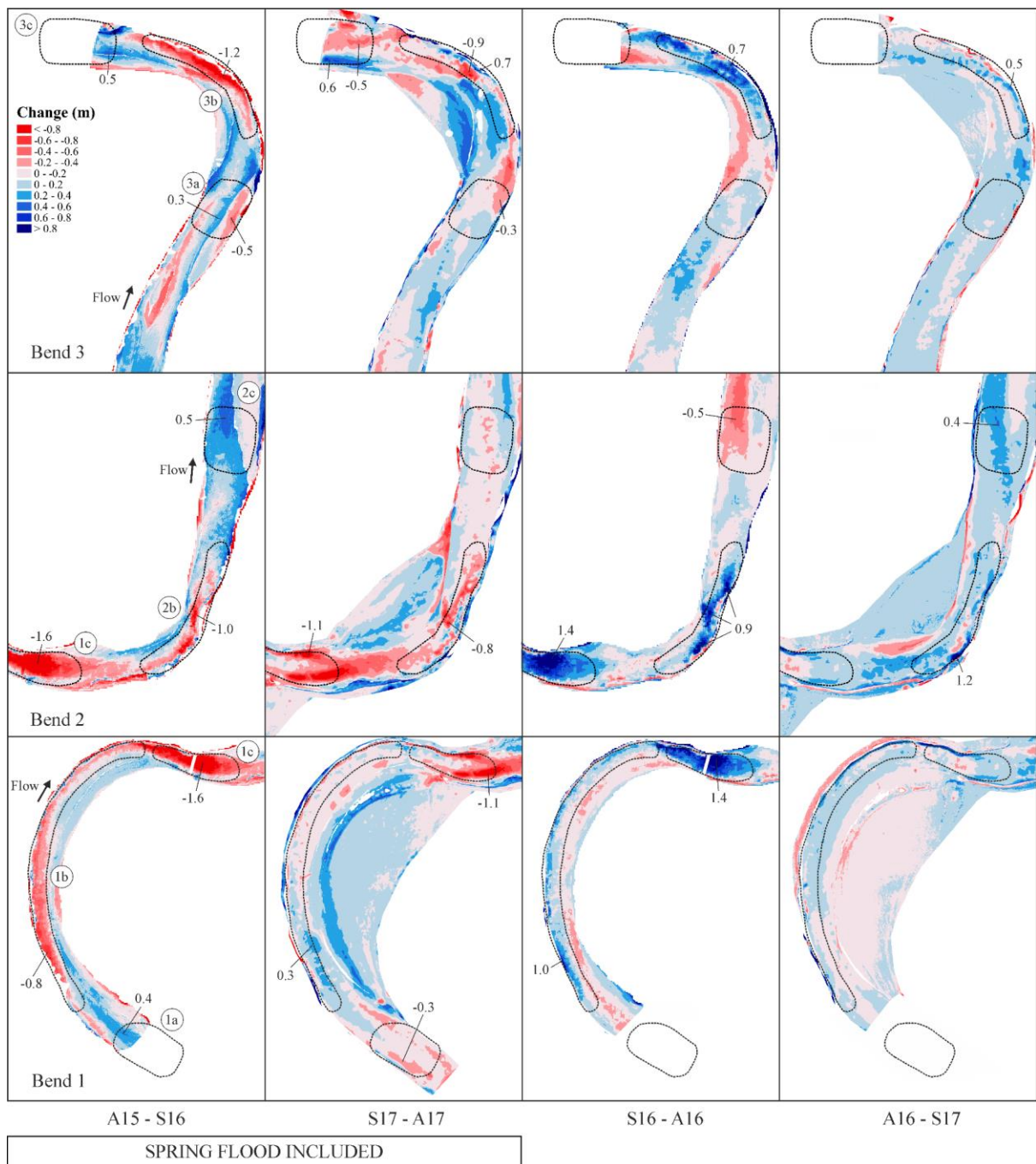
Figure 7. Seasonal morphological changes at meander bends during the study period. Meander bends are divided into different areas: (a) entrance, (b) concave side and (c) exit. The location of the strongest change at each area is marked with a value of vertical change during the time period. A= autumn, S = spring.

Table 6. Geomorphic units and the magnitude of strongest vertical change at each location during the study period. Geomorphic units are shown with a grey background, and vertical changes are shown

	A13	A13 - A14	A14	A14 - A15	A15	A15 - S16	S16	S16 - A16	A15 - A16	A16	A16 - S17	S17	S17 - A17	A16 - A17	TOTAL	A17
1a) Bend 1 entrance	R	-0.4/0.5	F	-0.3/0.5	R	0.4	R	No data	No data	No data	No data	R	-0.3	No data	-0.4/0.6	R
1b) Bend 1 concave side	F	0.7	F	0.3	F	-0.8	P	1.0	-0.5	F	-	F	0.3	-	0.6	F
1c) Bend 1 exit	P	-0.9/1.0	P	1.5	R	-1.6	P	1.4	-0.5	F	-	F	-1.1	-1.0	- 0.9/1.0	P
2b) Bend 2 concave side	P	1.1	P	0.7	P	-1.0	P	0.9	0.7	P	1.2	P	-0.8	-0.9/1.2	0.9	P
2c) Bend 2 exit	R	-0.3	F	-0.5	F	0.5	R	-0.5	-	F	0.4	R	-	-	-0.5	R
3a) Bend 3 entrance	F	0.3	F	-	F	-0.5/0.3	F	-	-0.3/0.3	F	-	F	-0.3	-	0.4	F
3b) Bend 3 concave side	P	1.5	F	-0.5/0.5	F	-1.2	P	0.7	-0.7	P	0.5	P	-0.9/0.7	-0.6/0.3	1.1	P
3c) Bend 3 exit	R	-0.6	F	-0.5/0.3	F	0.5	No data	No data	No data	No data	No data	F	-0.5/0.6	No data	-0.4	F

Based on our data, at low discharge, deposition can be extremely high in the areas that have eroded significantly before. For example, during the low discharge stage (see DoD S16 – A16 in Figs. 7 and 8), pools and concave sides were mainly filled while discharge remained under 10 m^3/s for the most part (Fig. 4). The strongest deposition areas were located on the concave sides of each bend (bend 1 = 0.6 m, bend 2 = 0.9 m and bend 3 = 0.7 m) and at the bend 1 exit (1.4 m). These areas were strongly eroded during the preceding time period. This finding is consistent with previous observations (e.g., Lane et al., 1996; Riley and Rhoads, 2012) that changes in river channels can occur outside the flood period during low-flow stages. Strong aggradation on concave sides and in pools may be explained by the fact that, below critical discharge, sediment particles entrained from riffles are deposited in pools owing to lower near-bed flow velocities. In addition, Vetter (2011) considered that pool filling is caused by flows not strong enough to carry the sediment towards the pool's downstream slope. Thus, the inflowing sediment exceeds the transport capacity in the pool and pool fills. During low discharges when near-bed flow velocities were slowest on the concave sides of the bends and at the bend 1 exit, the highest near-bed flow velocities were located at the inflexion points (Table 5), causing the strongest erosion at the exits of bends 2 and 3 (-0.5 m). These are the same locations where sediment was deposited during the preceding winter (including spring flood).

5.3. Morphological changes over consecutive years

Although DTM data were collected at the same time each autumn and each annual flow regime is characterized by spring flooding, there were no repetitive patterns between the years, and the riverbed

developed differently each year. During the first year, the concave sides of bends 2 and 3 and the bend 1 exit aggraded strongly, 1.1 m, 1.5 m and 1.0 m respectively. Simultaneously, areas of erosion were located at bend entrances and exits (1a = -0.4 m, 2c = -0.3 m and 3c = -0.6 m; Figs. 8 and 9, Table 6). In the second year, while concave sides of bend 2 and 3 remained quite stable or eroded (-0.5 m), respectively, instead of deposition, the strongest aggradation areas were located at the bend 1 exit (1.5 m) and entrance (0.5 m). During the third year, between autumn 2015 and autumn 2016, erosion was dominant at the bend 1 exit (-0.5 m) and the concave sides of bends 1 (-0.5 m) and 3 (-0.7 m), the same locations where the riverbed more or less aggraded during the preceding years. During the last year between autumn 2016 and autumn 2017, erosion areas were located at the concave sides of bend 2 (-0.9 m) and bend 3 (-0.6 m) and the bend 1 exit (- 1.0 m), similar to previous year. Differences in annual morphological changes may be explained by the timing and duration of the spring flood in relation to data acquisition. In addition, Vetter (2011) stated that flood-associated bedform accentuation is mainly controlled by the duration and not the magnitude of flows above the critical discharge. Findings regarding the nonlinear behaviour have been previously reported in terms of lateral change (Hooke, 2003; Gautier et al., 2010) and point bar and bank morphodynamics (Lotsari et al., 2014) of meandering rivers. Based on our results, vertical channel change can also be nonlinear (e.g., instead of continuous erosion). In addition, changes during similar hydrological conditions may differ from each other, because preceding morphological changes influence subsequent changes.
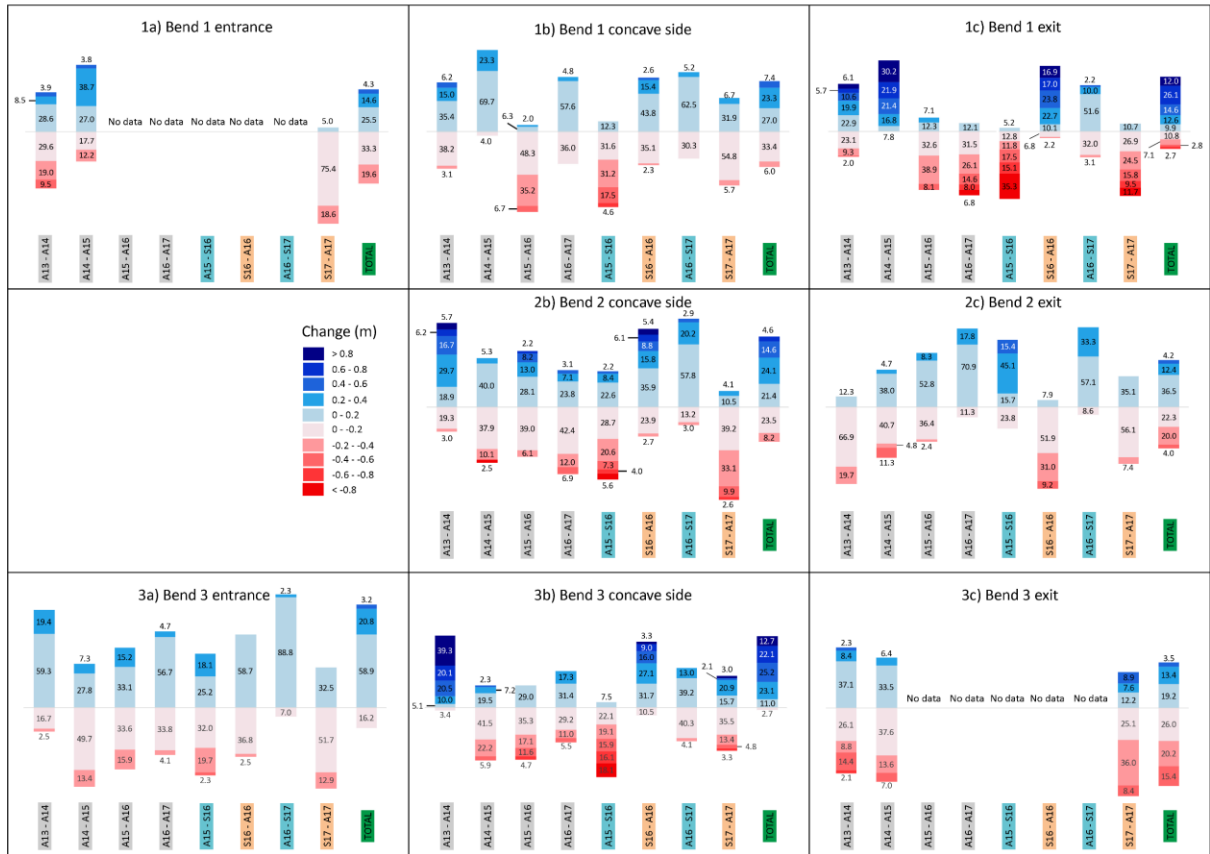
Figure 8. Percent change of each area (1a – 3c) during the study period. Area locations are shown in Fig. 1. Time periods are highlighted with coloured backgrounds: grey = annual, blue = winter, orange = summer and green = total change. Note that changes <2% of the total change have been omitted from the bar graphs. A = autumn and S = spring.
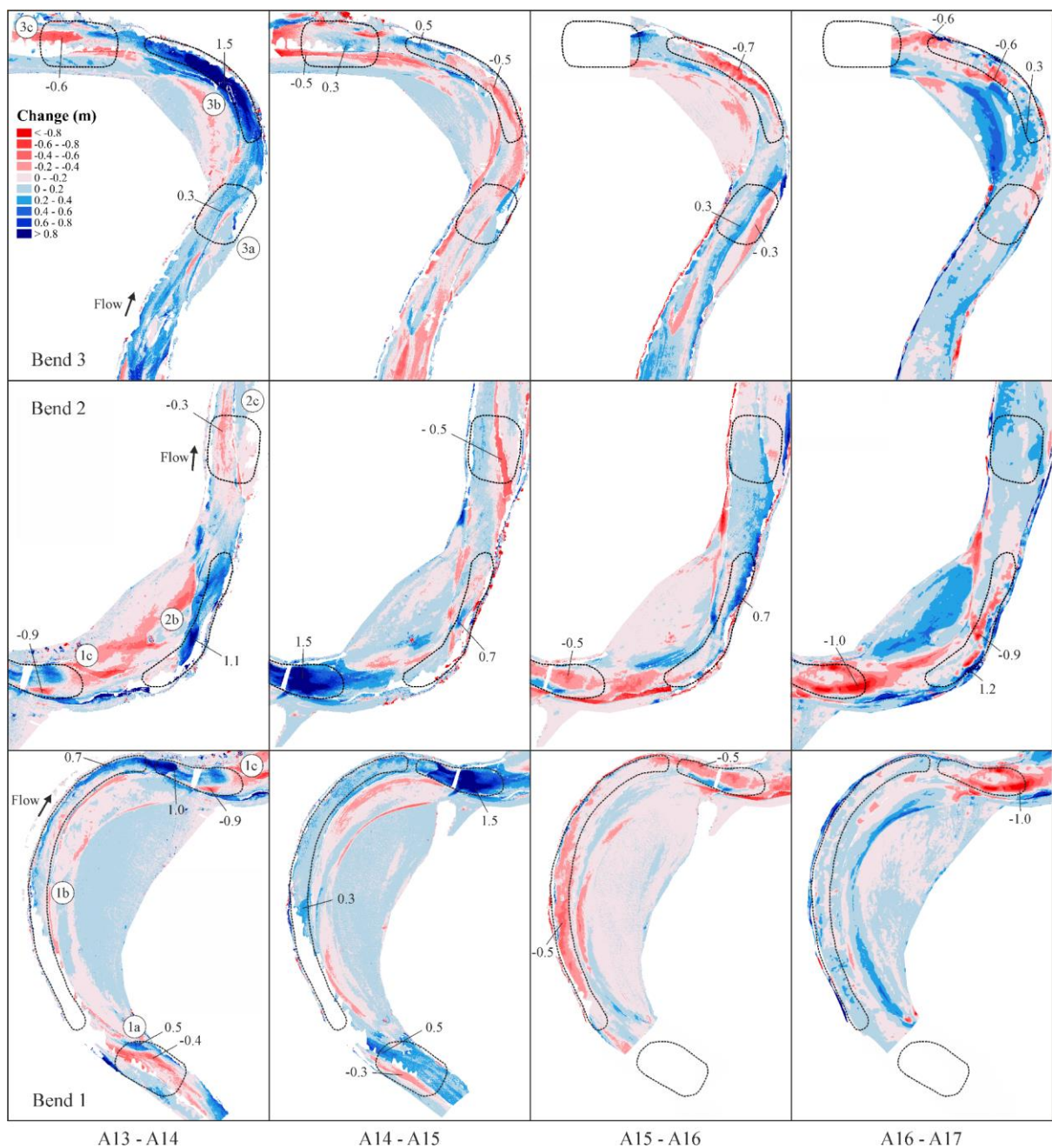
Figure 9. Annual morphological changes at meander bends between the autumns of 2013 and 2017. Meander bends are divided into different areas: (a) entrance, (b) concave side and (c) exit. The location of the strongest change at each area is marked with a value of vertical change during the time period. A= autumn.

The total change in bend topography between autumn 2013 and autumn 2017 is mainly characterized by aggradation on the concave sides of the bends and at the bend 1 exit, as well as erosion at the bend

1 entrance and the bend 3 exit (Fig. 10). Deep areas aggraded and shallow areas eroded. Concave sides of each bend (bend 1 = 0.6 m, bend 2 = 0.9 m and bend 3 = 1.1 m) and also the bend 1 exit (1.0 m) aggraded. Meanwhile, erosion was most dominant at the bend 1 entrance (-0.4 m) and the bend 2 (-0.5 m) and 3 (-0.4 m) exits. These areas were extremely shallow in autumn 2013. In addition, a large area of heavy erosion (-0.9 m) was located at the upstream part of bend 2's apex, which was shallow in autumn 2013. Despite the heavy deposition at pools on the concave side, none of the pools disappeared even though pool size changed. The total change at each bend was characterized by different time periods, rather than one significant flow event. Based on our data, pools are not always present at the concave sides of meander bends. Thus, concave sides may act as a temporary sediment storage (see e.g., DTM of 2014 and 2015 autumns in the appendix). However, storage is preserved only under effective hydrological discharge, which in our study is approximately 8 m³/s, ~20% of the bankfull discharge.
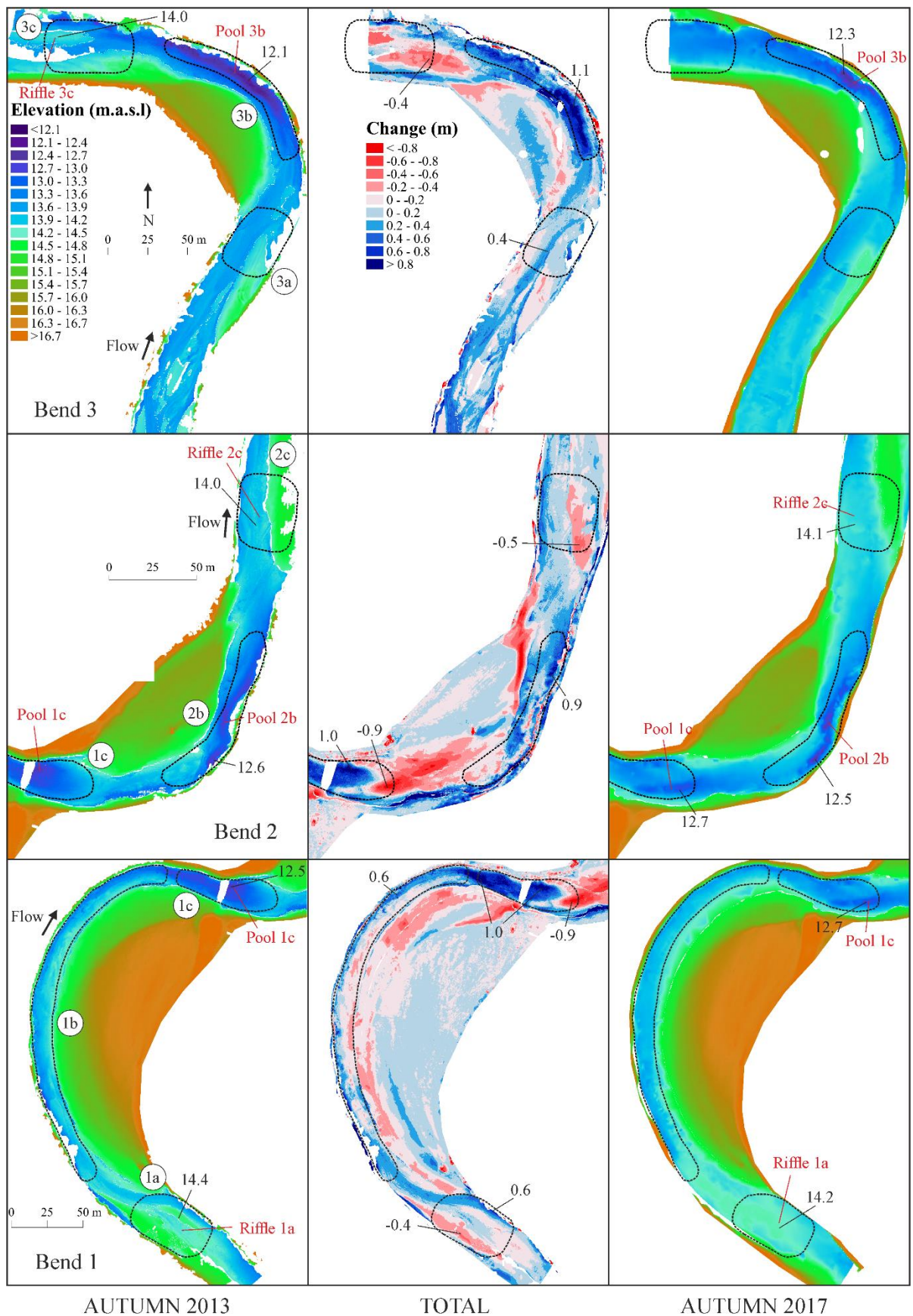
Figure 10. Morphological changes at meander bends over the study period. Meander bends are divided into different areas: (a) entrance, (b) concave side and (c) exit. DTMs (left and right columns) and DoD

(middle column) indicate geomorphic units and channel change. Pools, riffles and channel elevation (m.a.s.l.) are marked in the DTMs. In addition, the location of the largest change at each area is marked in DoDs with a value of vertical change (m) during the time period.

5.4. Riffle-pool sequences and maintenance

During high discharges we observed pool development on the concave sides of the meander bends and at the bend 1 exit, and riffle development at the inflexion points. Concave sides and inflexion points developed in the opposite direction during low discharges (i.e., pools filled and riffles eroded). Morphological changes of riffles and pools are linked. Riffles and pools developed simultaneously during the spring flood of 2016 and disappeared during the following summer and winter (Figs. 7 and 8, Table 6). During the spring flood, concave sides of bend 2 and 3 developed pools by eroding 1.0 m and 1.2 m, respectively, and riffles developed as bed elevations increased 0.5 m at the exits of bend 2 and 3. In the following summer, strong aggradation occurred at the same locations where erosion was strongest during the spring flood, leading to pool filling at each concave side. In addition, at the bend 2 exit where a riffle developed because of strong deposition during the spring flood, we observed erosion (-0.5 m). The linkage between riffles and pools was also found between the autumns of 2013 and 2014. While the concave sides of bends 2 and 3 and the bend 1 exit were strongly accretionary (1.1 m, 1.5 m and 1.0 m, respectively), filling pools, areas of strong erosion were located at bend exits and entrances (1a = -0.4 m, 2c = -0.3 m and 3c = -0.6 m; Figs. 8 and 9, Table 6), scouring riffles. It appears that the riffle–pool sequence is maintained if the discharge remains above critical discharge, which was ~8 m³/s (~ 20% of bankfull) in our study. Vetter (2011) also stated that the riffles and pool are maintained under the hydraulic conditions of high flow.

These findings indicate a clear link between riffle and pool development. This development has been linked in previous studies (Keller and Melhorn, 1978; Andrews, 1979; Thompson, 1986). Scour at the concave side`s pools can also lead to sediment deposition at point bar tails located downstream from the pools (Pyrce and Ashmore, 2005). In our study, riffle-pool dynamics were related to differences in

near-bed flow velocities between concave sides and bend entrances and exits as described in Section 5.1. Our dataset did not focus on potential sediment routing, described by Booker et al. (2001) and Milan (2013). However, our data shows that the HVC of near-bed flow is located next to concave sides at moderate flow (Fig. 5). Contrary to Milan´s (2013) conceptual model of sediment routing, the sediment is transported into the pools at low flows, filling them fully or partly. For pool formation, strong erosion must occur at concave sides at high flows, which is evident in our study. This erosion is caused by the HVC and secondary flow conditions at concave sides where near-bed flow velocities are higher than bend exits and entrances.

Thus, the longitudinal location of pools and riffles remained mostly the same during the study period, even though the size and shape was constantly changing, leading to deformation in some cases. These findings are similar to those of Vetter (2011) and Dury (1970) who stated that the position of riffles and pools remains the same. In addition, a pool developed on the concave side of bend 1 only once, during winter 2016 (including the spring flood), whereas pools usually developed on the concave sides of bend 2 and 3 and at the bend 1 exit. Only twice was a pool not located on bend 3's concave side: autumn 2014 and autumn 2015.

5.5. Morphological changes over consecutive meander bends

This study also documented that morphological changes in relation to discharge were rather similar among all meander bends and not just a feature of a particular bend. The study by Kasvi et al. (2013) on meander point bars supports our findings that similar changes occur among meander bends. However, our annual change detection reveals that changes are not always similar between adjacent meander bends. Local characteristics, such as bank failures, location along a river reach, backwater effects, and sediment grain size may cause differences in geomorphological change among bends (Lotsari et al., 2014; Konsoer et al., 2016b; Kasvi et al., 2017b). The inflexion point between meander bends 1 and 2 changed more extensively compared to other inflexion points. The areas of strongest morphological change were located mainly on the concave sides of each bend and at the bend 1 exit,

which was characterized by erosion protection and a suspension bridge (Fig. 1). The location of the pool at the bend 1 exit is not typical for a meandering river. However, Andrews (1979) stated that channel erosion occurs during peak discharge at locations where the cross section is more narrow. Erosion protection and the base of the suspension bridge, which narrowed the channel, most likely caused the exceptional development of the bend 1 exit. Because of this smaller cross-sectional width, based on flow continuity theory (Charlton, 2008, p. 76) the near-bed flow velocity and thus the erosion force increased faster in the bend 1 exit than at other inflexion points. Pool location can also be a consequence of changes in the HVC location. During high discharges, the HVC shifts from the outer bank towards the inner bank at the bend entrance and cuts across the point bar (Dietrich et al., 1979; Kasvi et al., 2015). Owing to the HVC shift and erosion protection, the HVC might collide with the outer bank at the bend exit with a steeper than normal angle. For example, Frothingham and Rhoads (2003) found that erosion is strongest at that location where flow is strongest at the outer bank and where the channel curvature varies locally (e.g., increases like in bend 1 exit). Because of erosion protection, the energy might have been directed towards the river bottom instead of the bank, which increased bed erosion and the development of pools. Bend 1 was characterized by the largest width during low-flow and bankfull discharges and demonstrated the highest rate of curvature (Table 1). Secondary circulation may not form with a large width-to-depth ratio (Leopold and Wolman, 1960; Termini and Piraino, 2011), and higher outer-bank roughness, caused by erosion protection in our study, may induce a zone of low velocity near the concave side (Konsoer et al., 2016a) and thus inhibit erosion near the concave side. This might explain why a pool was not always present at the concave side of bend 1 simultaneously with concave sides of bends 2 and 3 (Table 6, appendix).

5.6. Limitations and future research

Our demonstrated method allowed for more precise and reliable interpretations of spatial and temporal scales than have not been undertaken in previous studies. However, a few limitations exist related to data collection. First, because the reference and validation data for optical bathymetries (autumn 2013 – autumn 2015) were based on the accuracy of dGPS (1 m, horizontal), the depth sample may not represent exactly the same location as in the UAV images that were georeferenced with higher

accuracies. Second, ADCP-based bathymetries were modelled based on manual data collection. Therefore, point density is not the same along the study reach, and interpolated bathymetries do not represent the current situation along the river equally. However, these limitations did not have a significant influence on our study because we focused on meso-scale geomorphic units and change. Third, the number of near-bed flow velocity samples at each predefined area (1a – 3c) varies considerably between each measurement. However, we believe that averaging the samples at each area reduced the impact of the variability in the number of measurements.

Future research regarding the role of discharge on vertical channel adjustment should be carried out systematically within a single hydrological event (e.g., before and after the spring flood) to provide a more detailed understanding of the effects of various hydrological events on geomorphological change and riffle-pool maintenance. In addition, flow field measurements at various discharges could be conducted simultaneously with topography measurements to determine whether flow velocity and direction varies at different geomorphic units in different discharges. Annual flow data would be needed to understand annual change more precisely, but measurements under ice cover are difficult to conduct. For more detailed change detection purposes, ADCP-based bathymetries are more suitable than optical bathymetries.

6. Conclusion

This study was designed to evaluate morphological changes of riffle-pool sequences in three consecutive meander bends related to variations of discharge and near-bed flow velocity. The study focused on (1) morphological changes at meander bends and riffle-pool sequences related to flow variation and (2) similarities and dissimilarities between the consecutive meander bends and through time. The following conclusions can be drawn:

1) Variations of discharge and near-bed flow velocity exert important influences on morphological change and, thus, riffle–pool dynamics in meandering sand-bed rivers. During high flow stages, the riverbed is strongly eroded on the concave sides of meander bends, developing pools, while

deposition is dominant at the inflexion points, developing riffles. Meanwhile, during low flood stages, bend exits and, therefore, riffles are eroded, while pools on the concave sides are filled.
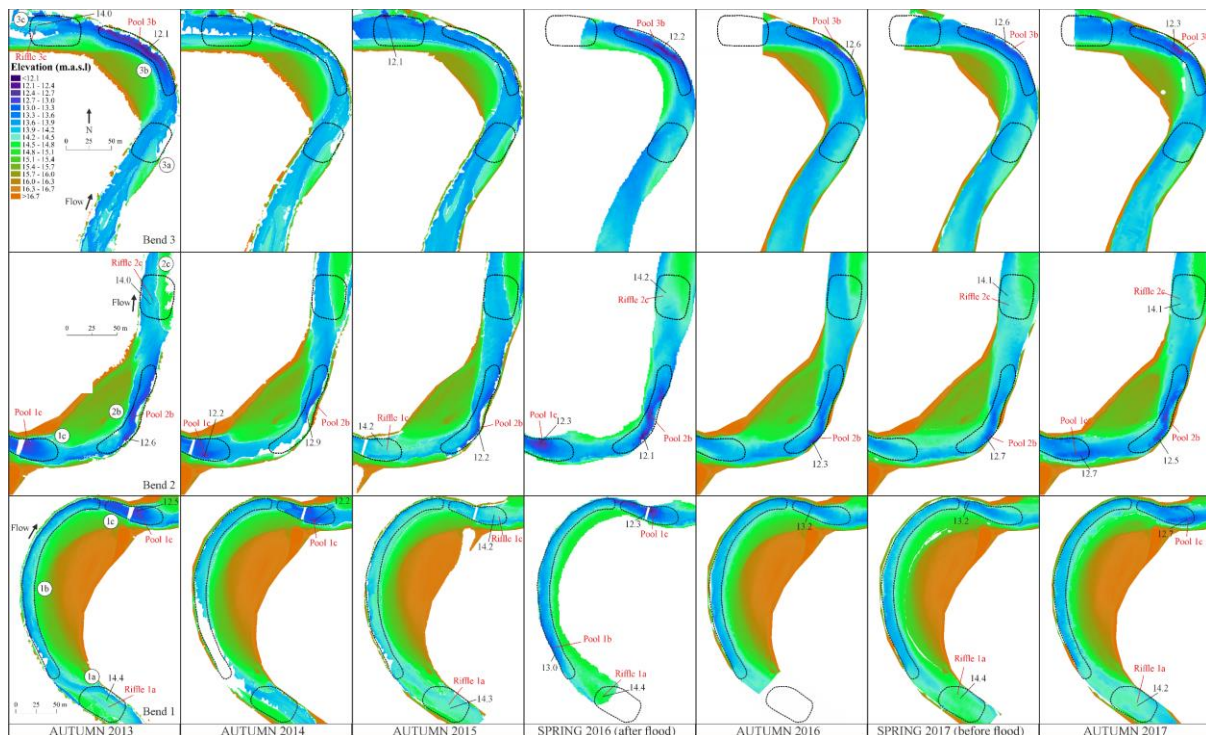
2) The riffle–pool sequence is maintained by effective hydrological events, in our study above ~20% of bankfull discharge. Below the effective discharge, water smooths the elevation differences in the riverbed and riffle-pool sequences disappear.

3) The geometry of meandering rivers contributes to the locations of riffles and pools. Geomorphic units remain stable in the longitudinal position, rather than migrating upstream or downstream. Pools and riffles are not, however, stable in size and shape.

4) As discharge increases, near-bed flow velocity increases faster on concave sides than at inflexion points. When ~20% of bankfull discharge is achieved, near-bed flow velocity becomes higher on concave sides than inflexion points, which explains why the areas with the most erosion are located on the concave sides and areas with the most aggradation are at inflexion points during floods.

5) Preceding morphological changes influence subsequent changes, and discharge and flow velocities are not the only factors that determine channel change.

6) Morphological changes are not linear from year to year. Vertical adjustment occurs year-round and is not limited to flood periods.

7) Meander bends with similar characteristics behave similarly. Erosion protection and suspension bridge structures (narrow cross-sectional areas) also have a strong influence on the vertical adjustment of the river channel.

8) Concave sides of meander bends may act as a temporary sink that stores sediment. However, storage is preserved only under effective hydrological discharge. In meandering sand-bed rivers, this effective discharge is much lower than gravel-bed rivers owing to finer bed sediment and thus smaller entrainment velocities.

Acknowledgements

Appendix

Supplementary data.

References

Alho, P., Kukko, A., Hyyppä, H., Kaartinen, H., Hyyppä, J., Jaakkola, A., 2009. Application of boat-based laser scanning for river survey. Earth Surf. Process. Landforms. https://doi.org/10.1002/esp.1879

Andrews, E.D., 1979. Scour and Fill In a Stream Channel, East Fork River, Western Wyoming. US Geol. Surv. Prof. Pap.

Axelsson, P., 2000. DEM generation from laser scanner data using adaptive TIN models. Int. Arch. Photogramm. Remote Sens. 33, 110–117.

Bathurst, J.C., Hey, R.D., Thorne, C.R., 1979. Secondary flow and shear stress at river bends. J. Hydraul. Div. 105, 1277–1295.

Blanckaert, K., 2010. Topographic steering, flow recirculation, velocity redistribution, and bed topography in sharp meander bends. Water Resour. Res. https://doi.org/10.1029/2009WR008303

Booker, D.J., Sear, D.A., Payne, a J., 2001. Modeling three-dimensional flow structures and patterns of boundary shear stress in a natural pool – riffle sequence. Earth Surf. Process. Landforms 26, 553–576. https://doi.org/10.1002/esp.210

Bridge, J.S., Jarvis, J., 1976. Flow and sedimentary processes in the meandering river South Esk, Glen Clova, Scotland. Earth Surf. Process. 1, 303–336.

Buffington, J.M., Lisle, T.E., Woodsmith, R.D., Hilton, S., 2002. Controls on the size and occurrence of pools in coarse-grained forest rivers. River Res. Appl. 18, 507–531. https://doi.org/10.1002/rra.693

Caamaño, D., Goodwin, P., Buffington, J.M., 2012. Flow structure through pool-riffle sequences and a conceptual model for their sustainability in gravel-bed rivers. River Res. Appl. https://doi.org/10.1002/rra.1463

Carling, P.A., 1991. An appraisal of the velocity-reversal hypothesis for stable pool-riffle sequences in the river severn, England. Earth Surf. Process. Landforms 16, 19–31. https://doi.org/10.1002/esp.3290160104

Carling, P.A., Harriet, G.O., 2000. Morphology of riffle-pool sequences in the River Severn, England. Earth Surf. Process. Landforms 25, 369–384. https://doi.org/10.1002/(SICI)1096-9837(200004)25:4<369::AID-ESP60>3.0.CO;2-M

Carling, P.A., Wood, N., 1994. Simulation of Flow over Pool-Riffle Topography - a Consideration of the Velocity Reversal Hypothesis. Earth Surf. Process. Landforms 19, 319–332. https://doi.org/DOI 10.1002/esp.3290190404

Charlton, R., 2008. Fundamentals of fluvial geomorphology. Routledge, London.

De Almeida, G.A.M., Rodríguez, J.F., 2011. Understanding pool-riffle dynamics through continuous morphological simulations. Water Resour. Res. 47. https://doi.org/10.1029/2010WR009170

Dietrich, W.E., Smith, D.J., 1984. Bed load transport in a river meander. Water Resour. Res. 20, 1355–1380.

Dietrich, W.E., Smith, J.D., Dunne, T., 1979. Flow and Sediment Transport in a Sand Bedded Meander. J. Geol. 87, 305–315. https://doi.org/10.1086/628419

Dury, G.H., 1970. A re-survey of part of the Hawkesbury River, New South Wales, after one hundred years. Aust. Geogr. Stud. 8, 121–132.

Ferguson, R., Ashworth, P., 1992. Spatial patterns of bedload transport and channel change in braided and near braided rivers. Billi , P., Hey, R.D., Thorne, C.R. Taconni , P., eds. Dyn. gravel-bed rivers. John Wiley Sons, Chichester 477–492.

Flener, C., 2013. Estimating deep water radiance in shallow water: Adapting optical bathymetry modelling to shallow river environments. Boreal Environ. Res. 18, 488–502.

Flener, C., Vaaja, M., Jaakkola, A., Krooks, A., Kaartinen, H., Kukko, A., Kasvi, E., Hyyppä, H., Hyyppä, J., Alho, P., 2013. Seamless mapping of river channels at high resolution using mobile lidar and UAV-photography. Remote Sens. 5, 6382–6407.

Flener, C., Wang, Y., Laamanen, L., Kasvi, E., Vesakoski, J.M., Alho, P., 2015. Empirical modeling of spatial 3D flow characteristics using a remote-controlled ADCP system: Monitoring a spring flood. Water (Switzerland). https://doi.org/10.3390/w7010217

Frothingham, K.M., Rhoads, B.L., 2003. Three-dimensional flow structure and channel change in an

asymmetrical compound meander loop, Embarras River, Illinois. Earth Surf. Process. Landforms 28, 625–644. https://doi.org/10.1002/esp.471

Fukushima, M., 2001. Salmonid habitat-geomorphology relationships in low-gradient streams. Ecology 82, 1238–1246. https://doi.org/10.1890/0012-9658(2001)082[1238:SHGRIL]2.0.CO;2

Gautier, E., Brunstein, D., Vauchel, P., Jouanneau, J.M., Roulet, M., Garcia, C., Guyot, J.L., Castro, M., 2010. Channel and floodplain sediment dynamics in a reach of the tropical meandering Rio Beni (Bolivian Amazonia). Earth Surf. Process. Landforms 35, 1838–1853. https://doi.org/10.1002/esp.2065

Hirsch, P.J., Abrahams, A.D., 1981. The properties of bed sediments in pools and riffles. J. Sediment. Res. 51, 757–760. https://doi.org/10.1306/212F7D9C-2B24-11D7-8648000102C1865D

Hodge, R.A., Sear, D.A., Leyland, J., 2013. Spatial variations in surface sediment structure in riffle-pool sequences: A preliminary test of the Differential Sediment Entrainment Hypothesis (DSEH). Earth Surf. Process. Landforms 38, 449–465. https://doi.org/10.1002/esp.3290

Hooke, J., 2003. River meander behaviour and instability: A framework for analysis. Trans. Inst. Br. Geogr. 28, 238–253. https://doi.org/10.1111/1475-5661.00089

Jaakkola, A., Hyyppä, J., Yu, X., Kukko, A., Kaartinen, H., Liang, X., Hyyppä, H., Wang, Y., 2017. Autonomous collection of forest field reference—The outlook and a first step with UAV laser scanning. Remote Sens. 9. https://doi.org/10.3390/rs9080785

Kasvi, E., 2015. Fluvio-Morphological Processes of Meander Bends – Combining Conventional Field Measurements , Close-Range Remote Sensing and Computational Modelling. Annales Universitatis Turkuensis, Turku.

Kasvi, E., Hooke, J., Kurkela, M., Vaaja, M.T., Virtanen, J.-P., Hyyppä, H., Alho, P., 2017a. Modern empirical and modelling study approaches in fluvial geomorphology to elucidate sub-bend-scale meander dynamics. Prog. Phys. Geogr. Earth Environ. 41, 533–569. https://doi.org/10.1177/0309133317715870

Kasvi, E., Laamanen, L., Lotsari, E., Alho, P., 2017b. Flow patterns and morphological changes in a sandy meander bend during a flood-spatially and temporally intensive ADCP measurement approach. Water (Switzerland) 9. https://doi.org/10.3390/w9020106

Kasvi, E., Salmela, J., Lotsari, E., Kumpula, T., Lane, S.N., 2019. Comparison of remote sensing based approaches for mapping bathymetry of shallow, clear water rivers. Geomorphology 333. https://doi.org/10.1016/j.geomorph.2019.02.017

Kasvi, E., Vaaja, M., Alho, P., Hyyppä, H., Hyyppä, J., Kaartinen, H., Kukko, A., 2013. Morphological changes on meander point bars associated with flow structure at different discharges. Earth Surf. Process. Landforms 38, 577–590. https://doi.org/10.1002/esp.3303

Kasvi, E., Vaaja, M., Kaartinen, H., Kukko, A., Jaakkola, A., Flener, C., Hyyppä, H., Hyyppä, J., Alho, P., 2015. Sub-bend scale flow-sediment interaction of meander bends - A combined approach of field observations, close-range remote sensing and computational modelling. Geomorphology 238, 119–134. https://doi.org/10.1016/j.geomorph.2015.01.039

Keller, E.A., 1972. Development of Alluvial Stream Channels: A Five-Stage Model. Geol. Soc. Am. Bull. 83, 1531–1536.

Keller, E.A., 1971. Areal sorting of bed-load material: The hypothesis of velocity reversal. Bull. Geol. Soc. Am. 82, 753–756. https://doi.org/10.1130/0016-7606(1971)82[753:ASOBMT]2.0.CO;2

Keller, E.A., Florsheim, J.L., 1993. Velocity-reversal hypothesis: A model approach. Earth Surf. Process. Landforms 18, 733–740. https://doi.org/10.1002/esp.3290180807

Keller, E.A., Melhorn, W.N., 1978. Rhythmic spacing and origin of pools and riffles. Bull. Geol. Soc. Am. 89, 723–730. https://doi.org/10.1130/0016-7606(1978)89<723:RSAOOP>2.0.CO;2

Knighton, D., 1998. Fluvial forms and processes. A New Perspective. Arnold, London.

Konsoer, K.M., Rhoads, B.L., Best, J.L., Langendoen, E.J., Abad, J.D., Parsons, D.R., Garcia, M.H., 2016a. Three-dimensional flow structure and bed morphology in large elongate meander loops with different outer bank roughness characteristics. Water Resour. Res. 52, 9621–9641. https://doi.org/10.1002/2016WR019040

Konsoer, K.M., Rhoads, B.L., Langendoen, E.J., Best, J.L., Ursic, M.E., Abad, J.D., Garcia, M.H., 2016b. Spatial variability in bank resistance to erosion on a large meandering, mixed bedrock-alluvial river. Geomorphology. https://doi.org/10.1016/j.geomorph.2015.08.002

Lane, S.N., Richards, K.S., Chandler, J.H., 1996. Discharge and sediment supply controls on erosion

and deposition in a dynamic alluvial channel. Geomorphology 15, 1–15. https://doi.org/10.1016/0169-555X(95)00113-J

Leopold, L.B., Wolman, M.G., 1960. River meanders. Geol. Soc. Am. Bull. 71, 769–793.

Leopold, L.B., Wolman, M.G., 1957. River channel patterns: braided, meandering, and straight. US Government Printing Office.

Leopold, L.B., Wolman, M.G., Miller, J.P., 1964. Fluvial Processes in Geomorphology. W.H. Freeman and Company, San Fransisco.

Lisle, T., 1979. A sorting mechanism for a riffle-pool sequence. Bull. Geol. Soc. Am. https://doi.org/10.1130/GSAB-P2-90-1142

Lotsari, E., Kasvi, E., Kämäri, M., Alho, P., 2017. The effects of ice cover on flow characteristics in a subarctic meandering river. Earth Surf. Process. Landforms 42, 1195–1212. https://doi.org/10.1002/esp.4089

Lotsari, E., Vaaja, M., Flener, C., Kaartinen, H., Kukko, A., Kasvi, E., Hyyppä, H., Hyyppä, J., Alho, P., 2014. Annual bank and point bar morphodynamics of a meandering river determined by high-accuracy multitemporal laser scanning and flow data. Water Resour. Res. 50, 5532–5559. https://doi.org/10.1002/2013wr014106

Lotsari, E., Wang, Y., Kaartinen, H., Jaakkola, A., Kukko, A., Vaaja, M., Hyyppä, H., Hyyppä, J., Alho, P., 2015. Gravel transport by ice in a subarctic river from accurate laser scanning. Geomorphology 246, 113–122. https://doi.org/10.1016/j.geomorph.2015.06.009

Lyzenga, D., 1981. Remote sensing of bottom reflectance and water attenuation parameters in shallow water using aircraft and Landsat data. Int. J. Remote Sens. 2, 71–82.

MacVicar, B.J., Roy, A.G., 2007. Hydrodynamics of a forced riffle pool in a gravel bed river: 1. Mean velocity and turbulence intensity. Water Resour. Res. 43. https://doi.org/10.1029/2006WR005272

Mansikkaniemi, H., Mäki, O.-P., 1990. Paleochannels and recent changes in the Pulmankijoki valley, northern Lapland. Fennia 168, 137–152.

Milan, D.J., 2013. Sediment routing hypothesis for pool-riffle maintenance. Earth Surf. Process. Landforms 38. https://doi.org/10.1002/esp.3395

Montgomery, D.R., Beamer, E.M., Pess, G.R., Quinn, T.P., 2011. Channel type and salmonid spawning distribution and abundance. Can. J. Fish. Aquat. Sci. 56, 377–387. https://doi.org/10.1139/f98-181

Nylén, T., Kasvi, E., Salmela, J., Kaartinen, H., Kukko, A., Jaakkola, A., Hyyppä, J., Alho, P (in press). Improving distribution models of riparian vegetation with mobile laser scanning and hydraulic modelling. PlosONE.

Pyrce, R.S., Ashmore, P.E., 2005. Bedload path length and point bar development in gravel-bed river models. Sedimentology 52, 839–857. https://doi.org/10.1111/j.1365-3091.2005.00714.x

Richards, K.S., 1976. The morphology of riffle-pool sequences. Earth Surf. Process. 1, 71–88. https://doi.org/10.1002/esp.3290010108

Riley, J.D., Rhoads, B.L., 2012. Flow structure and channel morphology at a natural confluent meander bend. Geomorphology 163–164, 84–98. https://doi.org/10.1016/j.geomorph.2011.06.011

Schumm, S.A., 1963. Sinuosity of Alluvial Rivers on the Great Plains. Geol. Soc. Am. Bull. 74, 1089–1100.

Schürch, P., Densmore, A.L., Rosser, N.J., Lim, M., McArdell, B.W., 2011. Detection of surface change in complex topography using terrestrial laser scanning: application to the Illgraben debris-flow channel. Earth Surf. Process. Landforms 36, 1847–1859.

Solinst, n.d. Solinst Levelogger Gold [WWW Document]. URL https://www.solinst.com/products/dataloggers-and-telemetry/3001-levelogger-series/operating-instructions/user-guide/1-introduction/1-1-7-levelogger-gold.php (accessed 1.23.19).

SonTek, 2010. RiverSurveyor S5/M9 System Manual [WWW Document]. URL http://www.facstaff.bucknell.edu/brh010/research/research/assets/RiverSurveyorLive Manual.pdf (accessed 1.23.19).

Termini, D., Piraino, M., 2011. Experimental analysis of cross-sectional flow motion in a large amplitude meandering bend. Earth Surf. Process. Landforms 36, 244–256.

Thompson, A., 1986. Secondary flows and the pool riffle unit: acase study of the processes of meander development. Earth Surf. Process. Landforms 6, 631–641.

Thompson, D.M., Wohl, E.E., 2009. The linkage between velocity patterns and sediment entrainment

in a forced-pool and riffle unit. Earth Surf. Process. Landforms 34, 177–192. https://doi.org/10.1002/esp.1698

Tonina, D., Buffington, J.M., 2009. A three-dimensional model for analyzing the effects of salmon redds on hyporheic exchange and egg pocket habitat. Can. J. Fish. Aquat. Sci. 66, 2157–2173. https://doi.org/10.1139/f09-146

Vetter, T., 2011. Riffle-pool morphometry and stage-dependant morphodynamics of a large floodplain river (Vereinigte Mulde, Sachsen-Anhalt, Germany). Earth Surf. Process. Landforms 36, 1647–1657. https://doi.org/10.1002/esp.2181

Wilkinson, S.N., Keller, R.J., Rutherfurd, I.D., 2004. Phase-shifts in shear stress as an explanation for the maintenance of pool-riffle sequences. Earth Surf. Process. Landforms 29, 737–753. https://doi.org/10.1002/esp.1066

Williams, R., Brasington, J., Vericat, D., Hicks, M., Labrosse, F., Neal, M., 2011. Monitoring braided river change using terrestrial laser scanning and optical bathymetric mapping, Developments in Earth Surface Processes. Elsevier B.V. https://doi.org/10.1016/B978-0-444-53446-0.00020-3

Williams, R.D., Brasington, J., Vericat, D., Hicks, D.M., 2014. Hyperscale terrain modelling of braided rivers: Fusing mobile terrestrial laser scanning and optical bathymetric mapping. Earth Surf. Process. Landforms 39, 167–183. https://doi.org/10.1002/esp.3437